Realization of a ^{87}Rb magneto-optical trap

Valerie Mauth

Bachelorarbeit in Physik
angefertigt im Institut für Angewandte Physik

vorgelegt der
Mathematisch-Naturwissenschaftlichen Fakultät
der
Rheinischen Friedrich-Wilhelms-Universität
Bonn

Januar 2023

Ich versichere, dass ich diese Arbeit selbstständig verfasst und keine anderen als die angegebenen Quellen und Hilfsmittel benutzt sowie die Zitate kenntlich gemacht habe.

Bonn, 23.01.2023 ..... V. Mauth .....

Datum Unterschrift

1. Gutachter: Prof. Dr. Sebastian Hofferberth
2. Gutachter: Prof. Dr. Stefan Linden

Acknowledgements

I would like to thank Prof. Sebastian Hofferberth for giving me the opportunity to write my thesis on this very interesting topic in the NQO group and for the interesting quantum optics lecture that made me aware of this group. I would also like to thank Prof. Linden for being the second corrector of this thesis. Furthermore, I want to thank Hannes Busche and Cedric Wind for the daily support during this thesis, for always answering all my questions and for new ideas and the constructive feedback. Thanks, for letting me be a part of the HQO group. A special thanks to Julia Gamper for always offering help, cheering me up when something did not work immediately and of course for the cookie breaks. Another thank you to the whole NQO group for the very nice working atmosphere and the daily lunch breaks. Finally, I want to thank my family and friends for always being there for me and believing in me no matter what.

Contents

1 Introduction **1**

2 Magneto-optical trap (MOT) for ^{87}Rb **3**
2.1 Magneto-optical trap . . . 3
2.1.1 Laser cooling . . . 3
2.1.2 MOT . . . 4
2.2 Laser cooling transitions for ^{87}Rb . . . 5
2.3 Experimental setup . . . 7
2.3.1 Vacuum chamber . . . 7
2.3.2 Magnetic field . . . 8
2.3.3 MOT light . . . 9

3 Laser system **10**
3.1 Laser locking . . . 10
3.1.1 Master laser . . . 11
3.1.2 Slave laser . . . 17
3.2 Light distribution . . . 19
3.2.1 Acousto-optical modulator (AOM) . . . 19
3.2.2 Fiber beam splitter . . . 21

4 Realization and imaging of a magneto-optical trap **23**
4.1 Absorption imaging . . . 23
4.2 Imaging setup . . . 25
4.3 Image acquisition . . . 25
4.4 Characterization of the imaging setup . . . 27
4.4.1 Power stability test . . . 27
4.5 First realization and imaging of the MOT . . . 30

5 Conclusion **32**

A Appendix **35**
A.1 Mode matching . . . 35
A.2 Adjustment of MOT beam polarization . . . 37
A.3 Time of flight (TOF) measurement . . . 39

Bibliography 40

CHAPTER 1

Introduction

Rydberg atoms have a wide variety of applications in, for example, quantum computing [1] or nonlinear quantum optics [2]. They offer electric dipole transitions over a broad range of the electromagnetic spectrum, ranging from optical to microwave. Furthermore, strong interactions between Rydberg atoms, including excitation blockade effects over many µm, can be observed [3, 4]. Many of their properties arise from the fact that Rydberg atoms possess strong transition dipole moments for microwave transitions between neighboring Rydberg states [1] which also renders them very sensitive to external microwave fields [5]. This makes Rydberg atoms prime candidates for realizing hybrid quantum systems that operate in both the optical and microwave regimes. One prerequisite to implement such systems is that the Rydberg atoms are cooled to some fraction of a Kelvin. This can be achieved using laser cooling and a combination of optical and magnetic trapping. Typically, the first step to do so is a magneto–optical trap (MOT) [6].
The Hybrid Quantum Optics (HQO) project aims to realize hybrid quantum systems based on the interaction between photons, highly excited Rydberg atoms and electromechanical oscillators in superconducting circuits [7]. In the experiment rubidium atoms are at first trapped and cooled down in a MOT [8]. Then the atoms will be conveyed via a magnetic transport [9] to the science chamber (see Fig. 1.1). The science chamber is planned as a cryostat with a 4K environment. The atoms will be trapped over an atom chip [10–12] and excited to Rydberg states with the aim to cool down a single mode of the mechanical resonator to its ground state through the interaction with the Rydberg atoms [13]. The cryostat is a prerequisite for the study of an electromechanical oscillator near its groundstate. It is also beneficial for the experiment since a better vacuum can be achieved without the need to bake out the chamber. Furthermore, the lifetime of the Rydberg atoms is increased [14] due to a reduced blackbody background [15]. The science chamber, where the actual experiment takes place, is separated from the MOT chamber where the rubidium atoms are initially laser cooled. The reason for this results from the aim to trap as much rubidium atoms as possible. This can be achieved with large beam diameters of the cooling light and by simply raising the partial rubidium pressure in the vacuum chamber. However, a high background pressure also increases the trap loss rates [16]. Most importantly, the cryostat requires radiation shields to block external black body radiation from the outside. For cooling and trapping the atoms in a MOT, large optical access ports would be required, which would increase the incident black body radiation and limit the cooling by the cryostat. That is why the HQO experiment uses a two-chamber system. The loading process happens in the MOT at relatively high background pressure and the atoms will then be transported to the cryogenic environment in the ultra-high vacuum science chamber.

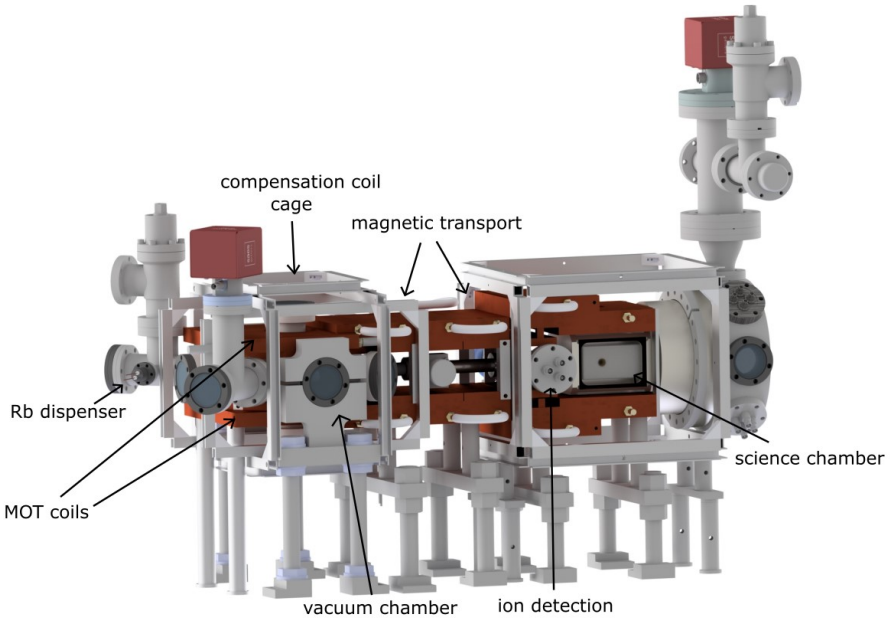

Figure 1.1: Illustration of the setup for the HQO experiment. The MOT is realized in the vacuum chamber on the left, where the atoms are initially cooled and trapped. They will then be moved by the magnetic transport to the science chamber where the cryostat will be and where the actual experiment will be performed. The image was made by Cedric Wind.

The aim of this thesis is the realization of the rubidium MOT as the first cooling step in the HQO experiment. Chapter 2 provides an overview of the theoretical concepts of a magneto-optical trap and a description of the vacuum chamber as well as of the magnetic fields and optical setup for realizing a MOT. Chapter 3 describes the laser system including frequency stabilization and light distribution of the cooler and repumper lasers. At first the laser locking process for stabilizing the two lasers in frequency and phase relative to a third laser, called master laser, is explained (see Section 3.1). Before the master laser can act as a reliable reference for the two slave lasers, it has to be locked to a reference cavity by using the Pound-Drever-Hall (PDH) [17] method (see Section 3.1.1). To be able to switch the cooler and repumper light on and off, three acousto-optical modulators (AOM) are implemented in the laser system (see Section 3.2.1). Furthermore, to evenly distribute the cooler and repumper light on the six MOT axes, fiber beam splitter are used (see Section 3.2.2). In Chapter 4 the principle of and optical setup for the absorption imaging of a MOT is explained. Since the MOT was only realized about a week before the end of this thesis, due to a delivery delay of the fiber beam splitters, there was no time to analyze and optimize the trapping properties of the MOT with absorption imaging. Therefore, only a characterization without trapped atoms was done (see Section 4.4) and first fluorescence and absorption images of the trapped rubidium atoms in the MOT are given in Section 4.5.

CHAPTER 2

Magneto-optical trap (MOT) for ^{87}Rb

The magneto-optical trap (MOT) in the HQO experiment is supposed to trap and cool as much rubidium atoms as possible before the atoms will be magnetically transported to the science chamber. The following chapter describes the working principle of a magneto–optical trap and the experimental setup for realizing a MOT in the HQO experiment where the vacuum chamber, the required magnetic fields and the optical setup for realizing a MOT will be explained.

2.1 Magneto-optical trap

In a magneto-optical trap atoms are laser cooled and, due to a quadrupole magnetic field, also confined in space [6]. In the following the working principle of a MOT is briefly summarized.

2.1.1 Laser cooling

The principle of laser cooling is based on the conservation of energy and momentum of light in a scattering process. An atom that is moving with a velocity $\vec{v}$ in one direction can be slowed down with a laser beam with wavevector $\vec{k}$ propagating in the opposite direction. For the moving atom the frequency ω_L of the counterpropagating photon is shifted to a higher frequency because of the Doppler shift. Therefore, in order for the atom to absorb a photon, the light must be red-detuned. The atom transitions to a higher energy state and experiences a recoil in the direction of the incident photon motion. After some time, the excited atom will spontaneously emit a photon and will return to the ground state. The spontaneous emission of a photon is isotropic which means that the photon is emitted in a random direction. Thus, the average momentum transfer of the spontaneous emission is zero which causes an average scattering force in the opposite direction of the incident atom motion [18]. To cool down an atom gas in one dimension two counterpropagating red-detuned laser beams have to be used. The resulting force F_{cooling} for one atom moving with velocity $\vec{v}$ is the difference between the scattering forces of the two laser beams. For a two-level atom it can be approximated with an expansion around small velocities v, what leads to [18]

$$F_{\text{cooling}} \approx \hbar k^2 \frac{8\delta}{\Gamma} \frac{I}{I_{\text{sat}}} \frac{1}{(1 + I/I_{\text{sat}} + (2\delta/\Gamma)^2)^2} v,$$

where I is the intensity of the light, I_{sat} is the saturation intensity, Γ is the natural linewidth of the atomic transition used for laser cooling and δ is the detuning of the cooling light frequency from the atomic transition frequency. For $\delta < 0$, which stands for red-detuned light, the resulting force is a damping force. It will slow down the atoms and the temperature will decrease. For the cooling process in three dimensions six laser beams, one counterpropagating pair for each dimension, are required. This is called optical molasses [18].

2.1.2 MOT

Optical molasses can cool atoms but is not able to confine them spatially. Using anti-Helmholtz coils, which create a spatially dependent quadrupole magnetic field with a uniform magnetic field gradient, can solve this problem[1]. The energy states of an atom in such a magnetic field will split up because of the Zeeman effect. The energy splitting depends on the magnetic quantum number m_F of the state and the magnitude of the magnetic field B. Consider a two-level atom with a hyperfine state with $F = 0$ as ground state and an excited degenerate state with $F = 1$ that will split into three states with $m_F = -1, 0, 1$ (see Fig. 2.1). Assume that an atom is located at $z > 0$ and is propagating in this direction. For $z > 0$ the

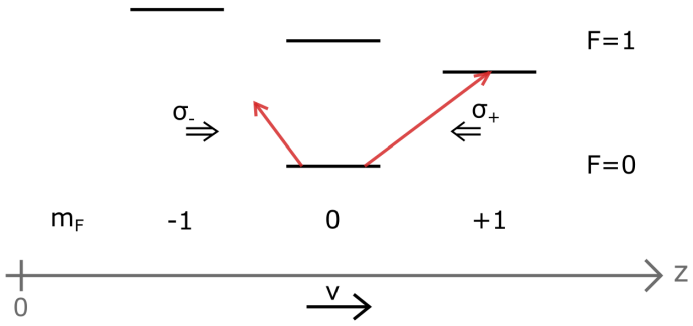

Figure 2.1: Zeemann splitting for a two-level atom, that propagates in the positive z–direction with velocity v, in a lineraly increasing external magnetic field for $z > 0$. A counterpropagating red detuned σ_+–polarized photon will be on resonance with the $\Delta m_F = +1$ transition due to the Doppler shift and Zeeman splitting. The red detuned σ_- photon is out of resonance.

magnetic field amplitude decreases, which causes the energy of the $m_F = +1$ state to decrease and the energy of the $m_F = -1$ to increase. If the atom is illuminated with two counterpropagating beams of different circular polarization, it will rather absorb a red-detuned counterpropagating σ_+ photon then a σ_- photon that is propagating in the same direction as the atom. It will push the atom back to the center and at the same time slow it down. This imbalance in the scattering force will occur in a similar way for an atom located on the negative z-axis. In both cases the atom will be pushed to the center of the trap [6, 18]. It is important to notice that $\sigma_\pm$ is defined with respect to the quantization axis in the atomic rest frame given by the direction of the magnetic field [18]. In contrast to this, the handedness of the polarization is defined relative to the direction of the propagation axis of the light. To drive the σ_+ transition in the cooling process all four beams in the (x, y)–plane have to be right-handed circularly

[1] Consider a setup as shown in Fig. 2.2. It follows from the Maxwell equation div $\vec{B} = 0$, that the magnetic field gradient in z–direction is twice the gradient in x– and y–direction [18]. That is why the z–axis is referred to as the strong axis in terms of the magnetic field gradient.

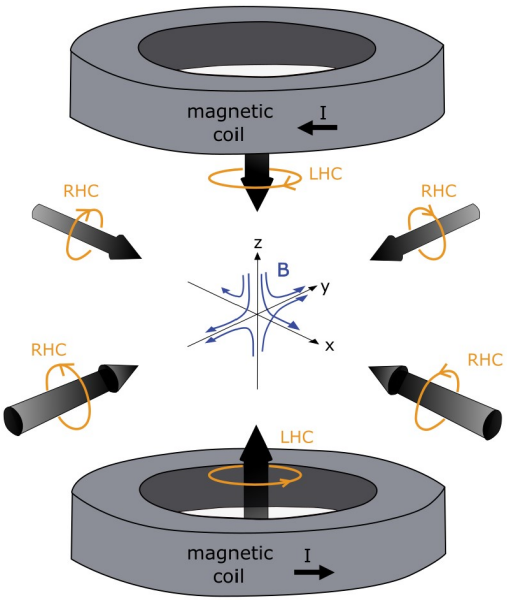

Figure 2.2: Schematic description of the operating mode of a MOT. Four right-handed circularly polarized (RHC) laser beams in the horizontal plane and two left-handed circularly polarized (LHC) laser beams in the vertical plane intersect in the center of the trap. A quadrupole magnetic field is generated by two magnetic coils with opposite current direction. The blue arrows indicate the direction of the magnetic field. The image is adapted from [18].

(RHC) polarized and the vertical beams have to be left-handed circularly polarized (LHC). The schematic description of a MOT is shown in Fig. 2.2.

The cooling process in a MOT is limited by the Doppler temperature. The spontaneous emission of a photon causes a recoil of the atom in a random direction. This results in a random walk of velocities what will heat up the atoms again [18]. However, this Doppler limit only applies for a two-level system. Atoms with a more complex energy structure, i.e. hyperfine structure, can be cooled to temperatures below the Doppler limit [19].

A MOT can only be realized in a vacuum chamber to reduce collisions between the trapped atoms and other particles. A collision could transfer enough energy to an atom so that it could escape the trap [19]. If the vacuum is sufficiently good, the main trap loss sourcees are light assisted collisions. The cooling light can excite two ground state atoms into either an attractive or a repulsive molecular potential [20]. When the atom pair is excited to the repulsive potential, the atoms push each other out of the trap.

2.2 Laser cooling transitions for ^{87}Rb

In Section 2.1 a two-level atom that gets cooled in a MOT was considered. However, rubidium has a more complex level structure, which is shown in Fig. 2.3. In the following the level structure and its implications for making a MOT are discussed. Rubidium is an alkali-metal atom and has one valence electron in the 5S–shell [18]. The only stable rubidium isotope is ^{85}Rb with an abundance of 72.17% [21]. Even though ^{87}Rb, with a lifetime of $4.88 \cdot 10^{10}$a, only has an abundance of 27.83%, the HQO experiment uses ^{87}Rb instead of ^{85}Rb [22]. The reasons for this are that ^{85}Rb has a more complex

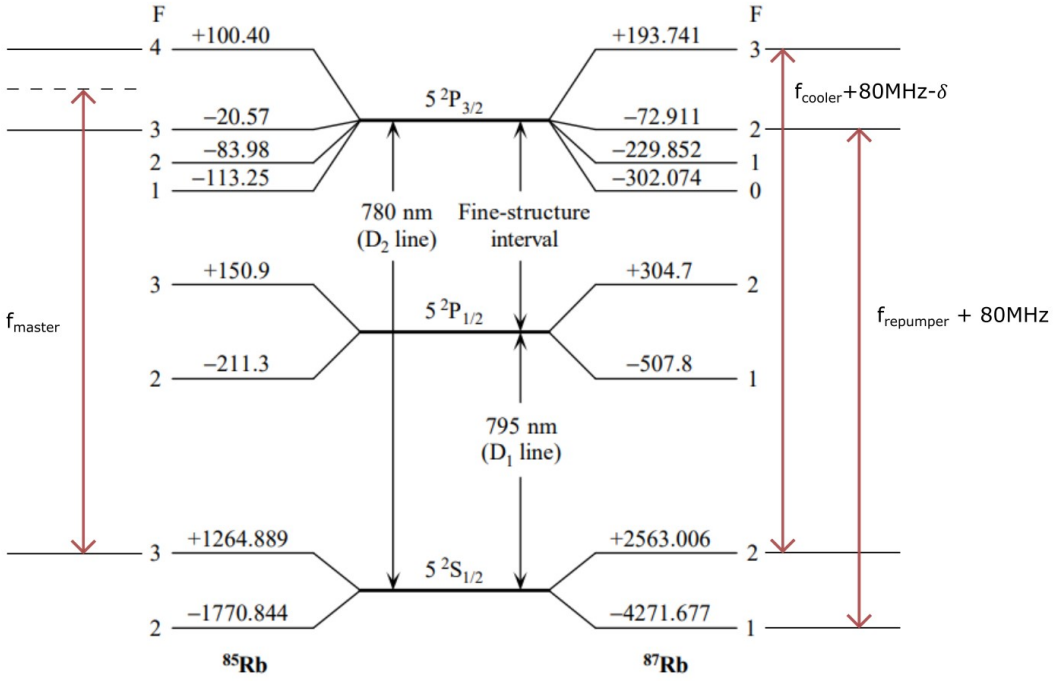

Figure 2.3: Level structure of ^{87}Rb and ^{85}Rb [24] with cooling and repumping transition and the crossover transition for locking the master laser (see Section 3.1.1). The frequency f of cooler and repumper are shifted around 80 MHz due to the AOM (see Section 3.2.1). The required red detuning of the cooler laser is described by δ.

hyperfine structure and evaporative cooling is less efficient for ^{85}Rb because of its different collision properties [23]. For the cooling process of ^{87}Rb the so-called cooler light excites the atomic transition from the ground state $[5S_{1/2}(F = 2, m_F = 2)]$ to $[5P_{3/2}(F = 3, m_F = 3)]$. After the atoms were excited to $[5P_{3/2}(F = 3, m_F = 3)]$, they spontaneously emit a photon and de-excite. The selection rules only allow the electron to fall back to the same ground state $[5S_{1/2}(F = 2, m_F = 2)]$. This is an important property of this transition because the atom cannot leave the cooling cycle during the spontaneous emission. To realize this the cooler laser has to be σ_+–polarized. At the beginning the σ_+–light also pumps the transitions from $[5S_{1/2}(F = 2, m_F = -2, -1, 0, 1, 2)]$ to $[5P_{3/2}(F = 3, m_F = -1, 0, 1, 2, 3)]$ until all atoms are in $[5P_{3/2}(F = 3, m_F = 3)]$, the starting point of the cooling cycle. This is called optical pumping and is necessary so that all atoms can take part in the cooling process [25]. However, during the absorption process there is a possibility to leave the cooling cycle. Because the cooler laser has a certain linewidth and is red detuned (δ) and its polarization is not perfect, it could happen that the atoms from the ground state $[5S_{1/2}(F = 2)]$ are excited to $[5P_{3/2}(F = 2)]$. These atoms could decay back to $[5S_{1/2}(F = 1)]$ and would no longer be part of the cooling process. A repumper laser that drives the transition $[5S_{1/2}(F = 1)] \rightarrow [5P_{3/2}(F = 2)]$ can solve the problem. The excited atoms can return, through spontaneous emission, to $[5S_{1/2}(F = 2)]$, which brings them back into the cooling cycle, or to $[5S_{1/2}(F = 1)]$. In the second case the repumper will excite the atom again to $[5P_{3/2}(F = 2)]$, and it will have another chance to come back to the cooling cycle.

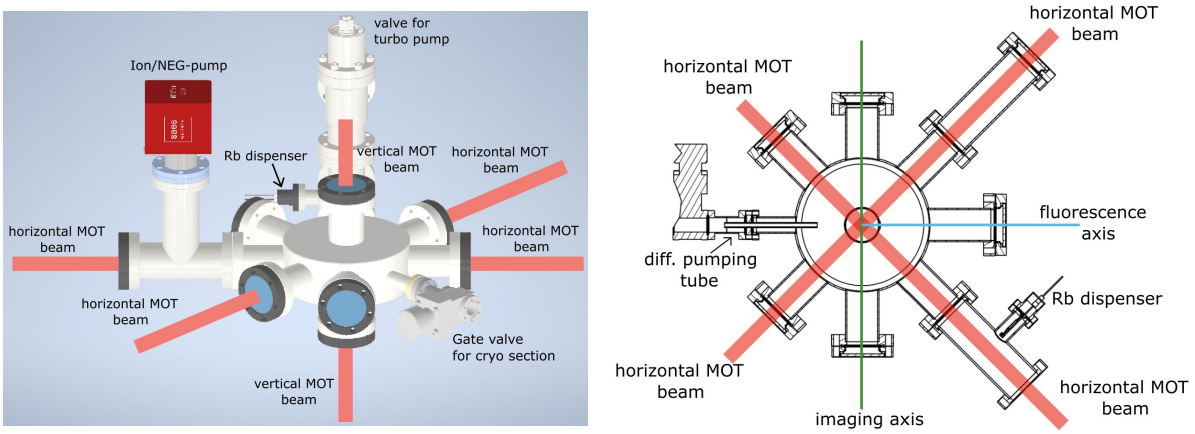

(a) (b)

Figure 2.4: **(a)** Illustration of the vacuum chamber. The red lines indicate the four horizontal and two vertical MOT beams. The vacuum in the chamber is created with the turbo pump and the ion/NEG-pump. The rubidium dispenser provides the rubidium atoms that will be trapped and cooled down. **(b)** Cross-section of the vacuum chamber. The imaging axis will be used for absorption imaging and on the fluorescence axis the spontaneously emitted cooling light can be observed. The differential pumping tube separates the MOT chamber with relatively high pressure from the science chamber at ultra-high vacuum. The drawings were made by Hannes Busche.

2.3 Experimental setup

The following paragraphs explain the experimental setup of the vacuum chamber, the required magnetic fields and the distribution of the MOT light.

2.3.1 Vacuum chamber

The magneto-optical trap in the HQO experiment is realized in a custom-made vacuum chamber[2] . An illustration of the vacuum chamber is shown in Fig. 2.4(a). The chamber has nine windows. Six of which are used for aligning the six MOT beams through the chamber. All MOT beams consist of cooler and repumper light achieved by using fiber beam splitters (see Section 3.2.2). Two of the remaining opposing windows are used for absorption imaging (see Chapter 4) and the last window is used for fluorescence imaging (see Fig. 2.4(b)). Fluorescence imaging means imaging the atom cloud by detecting the spontaneously emitted cooling light of the trapped atoms [16]. All the viewports, except for the one on the fluorescence axis, are anti-reflection (AR) coated for 780 nm to reduce the intensity loss due to reflection. To achieve a vacuum in the MOT chamber a turbo pump[3] is connected to the chamber. The turbo pump is responsible for an initial pump, which is followed by further pumping with a combined ion and non evaporable getter (NEG) pump[4] with a pumping speed of 200 l/s. With these two pumping stages a pressure of $\sim 2 \cdot 10^{-10}$mbar was reached. This pressure corresponds to the pressure calculated with the generated current in the ion pump. Thus, the pressure measured by the ion pump only depicts the properties directly at the pump. The pressure in the chamber is expected to be

[2] Custom-made vacuum chamber from VACOM [26]
[3] Turbo pump from PFEIFFER VACUUM [27]
[4] Ion-/NEG pump NexTorr Z 200 from SAES GETTERS [28]

slightly higher than this. To load the MOT with rubidium atoms a rubidium dispenser[5] is used. The dispenser consists of bismuth-rubidium compound (RbBi40 alloy) with 35 mg rubidium. By applying a current through the dispenser, the compound will heat up which causes the rubidium to evaporate into the vacuum chamber [29]. The MOT loading process increases the pressure in the MOT chamber again and the aim is to reach a pressure of $\sim 10^{-8}$mbar – 10^{-9}mbar dominated by the rubidium partial pressure. The differential pumping tube separates the MOT chamber with relatively high pressure from the science chamber at ultra-high vacuum where a pressure of 10^{-11}mbar is aimed at.

2.3.2 Magnetic field

To realize the quadrupole magnetic field, one magnetic coil is mounted on top and one on the bottom of the vacuum chamber. This is shown in Fig. 2.5 and Fig. 1.1. The two MOT coils carry current in opposite directions, called anti-Helmholtz configuration. The coils, with an outer diameter of 172 mm and an inner diameter of 74 mm, have 32 radial windings and two axial windings and create a quadrupole magnetic field with a magnetic field gradient of $\sim 2\,\mathrm{G/cm/A}$ along the strong axis. Here the 'strong axis' refers to the vertical axis. To control the current from the power supplies[6] through the MOT coils and in the future also the coils for the magnetic transport a home built switching box is used. The gradient can be increased or decreased by varying the current through the coils, what will be used for different MOT phases. The coils are mounted in water cooled blocks. Furthermore, three rectangular Helmholtz coil pairs, that produce an approximately homogeneous magnetic field [31], will be mounted around the vacuum chamber. These magnetic coils are used as compensation coils to compensate external magnetic fields like the Earth's magnetic field and provide a quantization axis during absorption imaging.

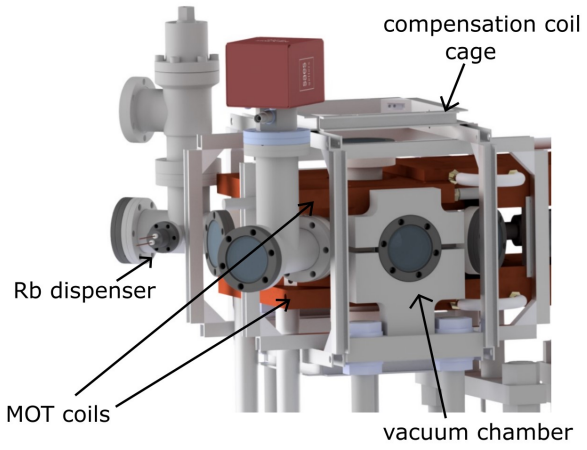

Figure 2.5: Illustration of the vacuum chamber in the HQO experiment with mounted anti-Helmholtz coil pairs and compensation coil cage. The drawing was made by Cedric Wind.

[5] Dispenser from AlfaVakuo e.U. [29]

[6] Power supplies from DELTA ELEKTRONIKA (SM66-AR-110, SM15-100 P218, SM15-100 P218) [30]

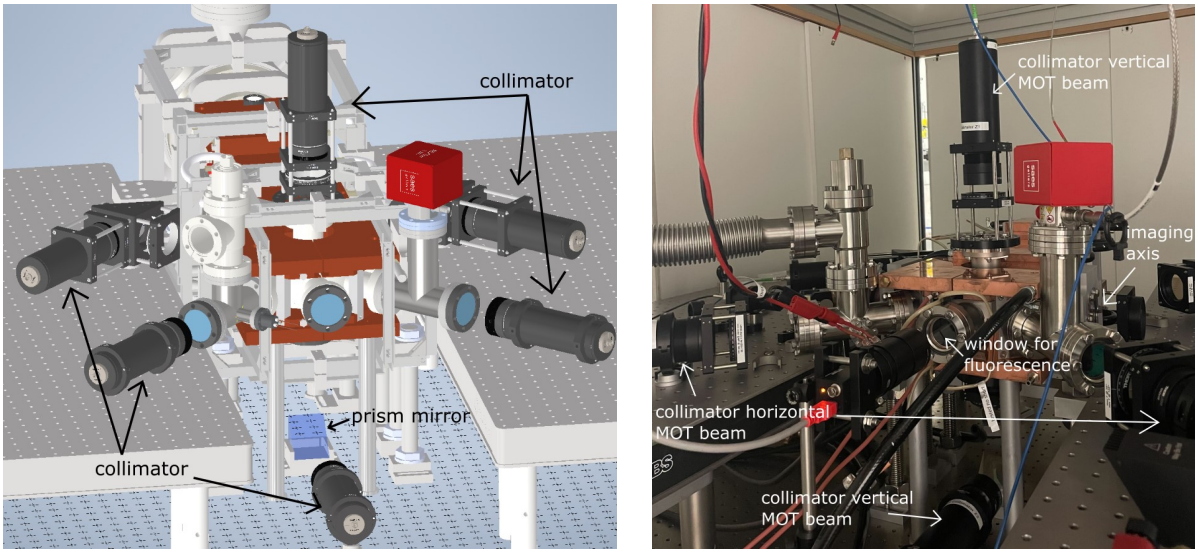

(a) (b)

Figure 2.6: **(a)** Illustration of the vacuum chamber in the HQO experiment. The light is guided with fibers to the MOT chamber and collimated with collimator lenses ($f = 200\,\text{mm}$) before the MOT beams are distributed along the six MOT axes. The bottom beam is guided over a prism mirror into the vacuum chamber. The drawing was made by Hannes Busche. **(b)** Picture of the current setup around the vacuum chamber in the HQO labor.

2.3.3 MOT light

The cooler and repumper light is guided through fibers to the MOT collimators. Collimator lenses ($f = 200\,\text{mm}$) behind the six fiber outputs, create collimated beams with a $1/e^2$ diameter of approximately 37.5 mm each. The reason for such large beam diameters is that the trapping rate of rubidium atoms in the MOT increases with the diameter [32]. Furthermore, an intensity of the cooler light above the saturation intensity is required to achieve high trapping rates. The saturation intensity of the cooling transition is $I_{\text{sat}} = 1.67\,\text{mW/cm}^2$ [22]. To address the correct cooling and repumping transitions, all of the six MOT beams have to be circularly polarized. The horizontal beam polarization needs to be of the opposite handedness to the vertical beam polarization. Since the output light of the fiber beam splitter is linearly polarized along one polarization axis of the fiber, a $\lambda/4$–plate (quarter-wave plate QWP) placed behind the collimator lens can produce circularly polarized light. The procedure for adjusting the handedness of the polarization of the MOT beams is explained in Appendix A.2. The setup for the vacuum chamber where also the collimators can be seen is shown in Fig. 2.6. The collimator for the bottom beam is placed on the optical table which is why the bottom beam has to be guided with the help of a prism mirror into the vacuum chamber.

CHAPTER 3

Laser system

Before the repumper and cooler light is coupled to the MOT collimators, it has to be stabilized in frequency and phase. To be able to switch the MOT beams on and off the light has to be modulated by AOMs, and cooler and repumper light have to be mixed by fiber beam splitters for aligning them together through the vacuum chamber. The implemented laser system for realizing this is explained in the following chapter. The laser locking system was already built once by Julia Gamper (see [25]). But because the HQO lab moved it had to be rebuilt, what was done in this thesis.

3.1 Laser locking

To be able to cool the atoms it is important that the frequency of the cooler and repumper laser matches the transition frequency of the cooling and repumping transition in the atom and has a small linewidth, of the order of the atomic linewidth. Hence, the frequency of the cooler laser must be stabilized to $[5S_{1/2}(F = 2, m_F = 2) \rightarrow 5P_{3/2}(F = 3, m_F = 3)]$ of ^{87}Rb and the frequency of the repumper laser has to be stabilized to $[5S_{1/2}(F = 1) \rightarrow 5P_{3/2}(F = 2)]$ of ^{87}Rb. The frequency stabilization of the two slave lasers (cooler and repumper) is done with a third laser, the so-called master laser, that acts as a reference. The master laser is stabilized in frequency by locking the laser to a reference cavity with the Pound–Drever–Hall (PDH) method [17]. It is locked at the cross–over resonance $[5S_{1/2}(F = 3) \rightarrow 5P_{3/2}(F = 3, 4)]$ of ^{85}Rb. Superimposing slave laser and the stabilized master laser creates a beat note signal that can be used for stabilizing the slave laser at the required frequency offset to the master laser. The methods and implementations for locking master and slave laser will be explained in the following.

In the HQO experiment 'external cavity diode lasers' (ECDL) in Littrow configuration are used. For the Littrow configuration a collimating lens and a diffraction grating is placed behind the diode laser output (see Fig. 3.1). The diffraction grating is positioned in such a way, that the first order diffraction is reflected to the diode laser and acts as an optical feedback signal, whereas the zeroth-order diffraction forms the output beam. Rotating the diffraction grating and varying its distance to the diode laser with a piezo actuator causes a change in the wavelength of the output light [33]. This is used for coarse tuning and scanning the wavelength of the laser. Changing the laser diode current also influences the wavelength of the output light, which can be used for fine tuning the wavelength [34]. An overview of the lasers that are used in the HQO experiment is given in Table 3.1. The TApro1 laser has a main and a

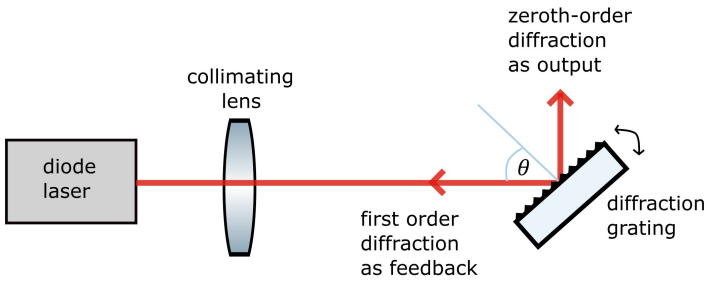

Figure 3.1: Schematic representation of a diode laser in Littrow configuration. The first order diffraction is reflected to the diode as an optical feedback. The zeroth-order diffraction forms the output beam. The position of the grating can be changed with a piezo actuator. The figure is modeled after [35].

Table 3.1: Overview of the lasers that are used in the HQO experiment, and their atomic transitions and corresponding wavelengths to which they are locked.

name	laser	atomic transition	wavelength
master	DLpro1[1]	^{85}Rb: $5S_{1/2}(F=3) \rightarrow 5P_{3/2}(F=3,4)$	780.2439 nm
cooler	TApro1[2]	^{87}Rb: $5S_{1/2}(F=2, m_F=2) \rightarrow 5P_{3/2}(F=3, m_F=3)$	780.2460 nm
repumper	DLpro2[3]	^{87}Rb: $5S_{1/2}(F=1) \rightarrow 5P_{3/2}(F=2)$	780.2327 nm

side output. The side output provides light with lower power (18.5 mW) and the main output provides light with higher power (3 760 mW). DLpro1 and DLpro2 send out light with a power of 108 mW. An optical isolator that prevents back reflections, which could damage the laser diode, is integrated in each laser [34].

3.1.1 Master laser

The master laser is locked to the reference cavity by using the Pound–Drever–Hall (PDH) method [17]. To make sure that the master laser is locked at the cross-over resonance $[5S_{1/2}(F=3) \rightarrow 5P_{3/2}(F=3,4)]$ of ^{85}Rb, a frequency reference is needed. The measurement of the wavelength with the wavemeter[4] of the HQO group is not precise enough since it only has an absolute accuracy of 200 MHz. Therefore, the Rubidium spectrum, obtained by Doppler-free saturation spectroscopy, is used as a reference for the locking process of the master laser.

3.1.1.1 Doppler-free saturation spectroscopy

The resolution of laser spectroscopy is usually limited by the Doppler broadening. With the Doppler-free saturation spectroscopy it is possible to do a more precise measurement, where the hyperfine structure gets visible. Two laser beams with the same tunable frequency ω but different intensities must propagate antiparallel through the atom cloud. The laser with higher intensity is called 'pump laser' and the other one 'probe laser'. For atoms with velocity $\vec{v}$ the frequency ω of the pump laser is Doppler shifted so it can only excite atoms with transition frequency ω_0 if $\omega = \omega_0 + \vec{k}\vec{v}$, where $\vec{k}$ is the wavevector.

[4] WS6-200 Series High Precision Wavemeter from HighFinesse [37]

Since pump and probe laser are propagating in opposite directions, they will be absorbed by atoms with different velocities $\vec{v}$. Only in the case of $\omega = \omega_0$ the two beams are resonant with the same atoms, that have a velocity component of zero parallel to the beam. The pump beam will be absorbed by the atoms and reduces the population in the ground state. The atomic transition will be saturated, and the probe beam will be absorbed less which causes a peak in the transmission signal of the probe laser. The width of this peak is about two magnitudes smaller than the Doppler broadening [38]. In a Doppler-free saturation spectrum there are peaks observable that do not belong to an atomic transition. These so-called 'crossover transitions' can occur when the atom has two excited states with a frequency difference smaller than the Doppler broadening, and a common ground state. Furthermore, the laser frequency ω has to be between the two transition frequencies ω_1 and ω_2. There are atoms with velocity $\vec{v}$ that cause a Doppler shift of the pump beam frequency to ω_2 and of the probe beam to ω_1, and also the other way around for velocity $-\vec{v}$. In both cases the pump beam causes a reduction of the ground state population that leads to an additional peak in the transmission signal of the probe beam [39].

The setup in the HQO experiment for the Doppler-free saturation spectroscopy of rubidium is shown in Fig. 3.2. The $\lambda/2$–plates and the polarizing beam splitter (PBS) split the light in different beams with adjustable power. The light is then coupled to a polarization maintaining fiber (PMF) and will be guided to the actual setup for Doppler-free saturation spectroscopy. The fiber output gets reflected in the PBS and illuminates the rubidium reference cell. The reference cell contains vapor of ^{87}Rb and ^{85}Rb. The telescope in front of the Rb cell is used to widen the beam so that the photons interact with as many atoms as possible. The light then passes a $\lambda/4$-plate, gets reflected on a mirror and passes again the $\lambda/4$-plate. Two consecutive $\lambda/4$-plates act like a $\lambda/2$-plate that rotates the polarization axis of the incoming light about 90°. After that the light goes again through the Rb cell. When the light passes the cell the first time, it acts as the pump beam with high intensity. The second time the intensity is lower because some of the photons were already absorbed. The beam now acts as the probe beam. Since the polarization axis of the light was rotated, the probe beam gets transmitted in the PBS and can be detected on the photodiode. The photodiode is connected to an oscilloscope where the transmission signal of the probe beam can be displayed. The Rb spectrum, that was recorded with this setup, is shown in Fig. 3.3.

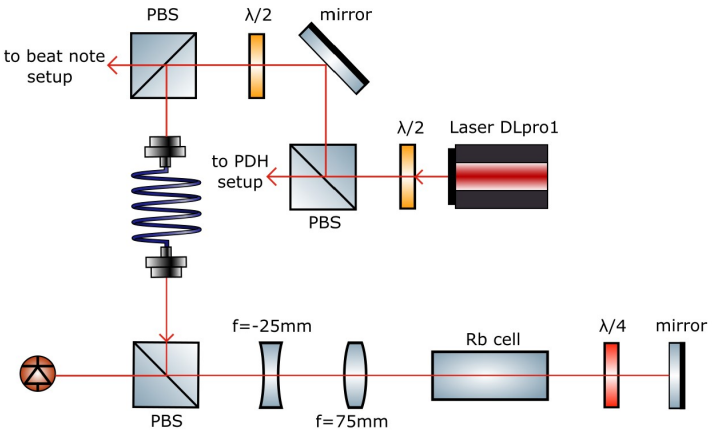

Figure 3.2: Optical setup for the Doppler-free saturation spectroscopy. The beam gets reflected at the PBS and passes the Rubidium cell as 'probe beam'. It gets reflected at the mirror and traverse the Rubidium cell again. The beam will then be transmitted through the PBS and detected on a photodiode.

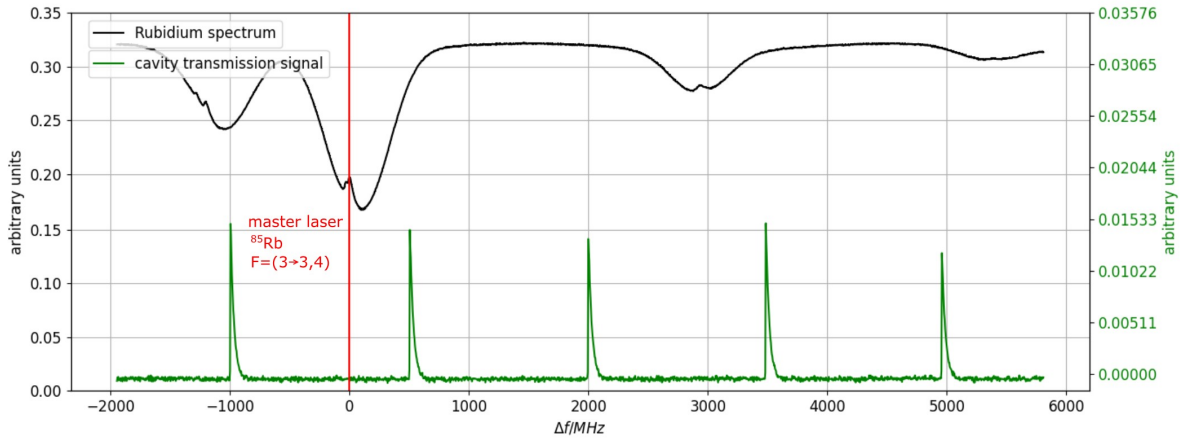

Figure 3.3: Rubidium spectrum of the $5S_{1/2} \rightarrow 5P_{3/2}$ transition, obtained with Doppler-free saturation spectroscopy. The red line indicates the cross-over transition to which the master laser is stabilized. The $x-$axis is given in units of Δf what denotes the frequency difference to the cross-over transition frequency. Furthermore, the transmission signal, generated by a photodiode behind the cavity, is shown (see Section 3.1.1.3).

3.1.1.2 Pound–Drever–Hall (PDH) method

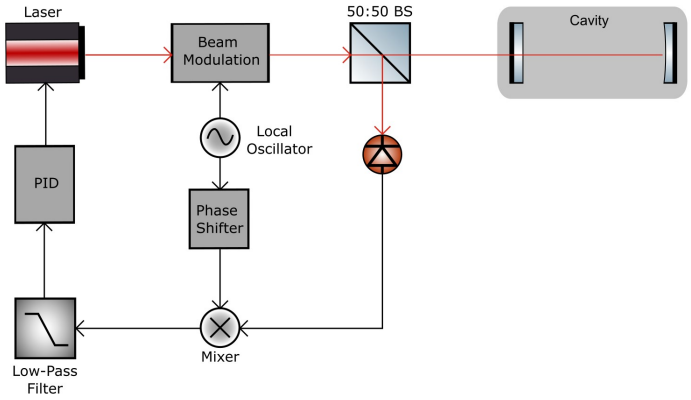

Figure 3.4: Schematic setup for implementing the Pound–Drever–Hall (PDH) method [17]. The red lines describe the path of the light, and the black lines describe the path of the electronic signal. The figure is modeled after [17].

Light that is sent through a cavity produces peaks in the transmission signal and a minimum in the reflection signal if the cavity length L is equal to an integer number of half the wavelength of the light. If the wavelength and accordingly the frequency fluctuates around the resonance frequency of the cavity, the transmission signal decreases and the reflection signal increases proportionally. The transmission and reflection signal are a measure of the deviation of the incident light frequency from the resonance frequency. The problem is that both signals are symmetric about resonance, so it is not possible to determine to which side of the resonance frequency the laser is drifting. The PDH method uses the fact that the derivative and the phase of the reflection signal is antisymmetric about resonance to create an error signal that is fed back to the laser to hold the frequency on resonance [17].

To get such an error signal the phase of the laser beam, described as $E = E_0 e^{i\omega t}$ (ω: laser frequency,

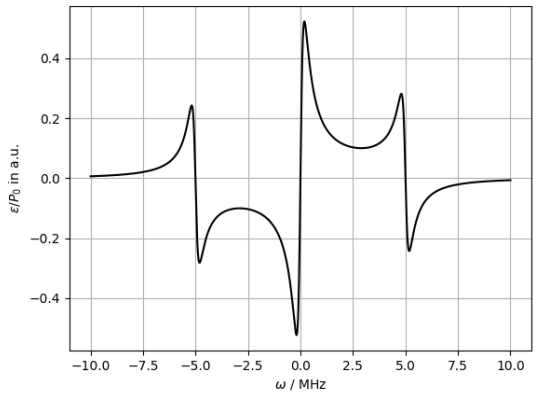

Figure 3.5: Theoretical error signal for a cavity with $\Delta_{\mathrm{FSR}} = 1.497\,\mathrm{GHz}$, $R = 0.99987546$ and sidebands at $\Omega_{\mathrm{PDH}} = \pm 5\,\mathrm{MHz}$. These values correspond to the actual values for the used cavity in the HQO experiment.

here also called carrier frequency; E_0: amplitude), has to be modulated in phase. The modulation, driven by a signal generated from the local oscillator (see Fig. 3.6) with phase modulation frequency Ω_{PDH} will create two additional signals around the carrier. These signals with frequency $\omega + \Omega_{\mathrm{PDH}}$ and $\omega - \Omega_{\mathrm{PDH}}$ are called sidebands. This modulated beam is then coupled to the cavity as shown in Fig. 3.4. The reflection on the first mirror of the cavity causes interference of the carrier with the sidebands and interference of the sidebands with each other [17]. The interference of the carrier with the sidebands depends on the phase of the reflected beam, which gives information about the side to which the frequency is drifting. To isolate this interference signal, the photodiode signal and the local oscillator signal, which is phase shifted to compensate possible delays in the two paths, are fed into the mixer and its output signal then passes a low-pass filter. At high modulation frequencies ($\Omega_{\mathrm{PDH}} \gg \Delta_{\mathrm{FSR}}/\mathcal{F}$, with $\mathcal{F}$ being the Finesse of the cavity) the sidebands are far away from resonance what causes them to be mostly reflected. This will lead to an error signal ε that is linear about resonance (see Fig. 3.5) [17]

$$\varepsilon = -2J_0(\beta)J_1(\beta)P_0\Im\mathfrak{m}\{F(\omega)F^*(\omega+\Omega) - F^*(\omega)F(\omega-\Omega)\} \tag{3.1}$$

where J_n are the Bessel functions, P_0 is the power of the incident beam and F is the reflection coefficient. This error signal will be put into a PID controller and the output will be fed back to the laser to hold the frequency on resonance.

3.1.1.3 Coupling to the cavity

For the PDH method the master laser has to be coupled into the reference cavity. The goal is to couple to the fundamental transverse TEM_{00} mode. This mode describes a laser beam with a Gaussian intensity distribution in the transverse plane. The width $w(z)$ and radius of curvature $R(z)$ of the beam evolve along the propagation axis z. The minimal width is given by the beam waist w_0 [40]. The cavity used in the HQO experiment is a Ultra Low Expansion (ULE) resonator[5] with a plane mirror ($R_1 = \infty$) and a concave mirror ($R_2 = -500\,\mathrm{mm}$) and a measured Finesse of $\mathcal{F} = 21500 \pm 200$ [25]. Mode matching of

[5] ATF 6020-4 from Stable Laser Systems [41]

the incident beam is achieved when the waist w_0 is located at the plane mirror and the radius of curvature of the wavefront corresponds to the radius of the concave mirror [42]. For more information concerning the mode matching see Appendix A.1.

The setup used for the mode matching is shown in the gray area of Fig. 3.6. The modulation of the sidebands with the electro–optical modulator (EOM) is turned off for the coupling. The first lens is used to collimate the beam from the fiber and the second lens is used to focus the beam so that the beam waist w_0 has the right size and is located at the position of the plane mirror. The PBS and dichroic mirror will be used in the future to couple a second laser for the Rydberg excitation to the reference cavity. A photodiode is placed behind the cavity to observe the transmission signal. By optimizing the alignment, the transmission of higher order modes can be reduced so that the transmission signal of the fundamental mode dominates. The procedure for coupling light into the cavity is described more precisely in [42]. In the HQO setup a ratio of 1% of transmission from the higher order modes compared to the transmission of the fundamental mode was reached. The photodiode signal after optimization of the coupling can be seen in Fig. 3.3. The frequency spacing between the two transmission peaks is given by the free spectral range $\Delta_{\mathrm{FSR}} = c/(2L) = 1.497\,\mathrm{GHz}$, where $L = 100.1\,\mathrm{mm}$ is the length of the cavity and c the speed of light.

As one can see in Fig. 3.3 the frequency of the fundamental mode does not coincide with the cross–over resonance $[5S_{1/2}(F = 3) \rightarrow 5P_{3/2}(F = 3, 4)]$ of ^{85}Rb. Since the master laser will be locked at this cross–over transition, a resonance of the cavity at this frequency is needed. This can be achieved with a fiber-EOM[6] that modulates, in addition to the sidebands for the PDH method, strong sidebands to the fundamental mode. With a modulation signal of 507 MHz the strong sideband at the -1$^{\mathrm{st}}$ order can be shifted to the cross–over frequency.

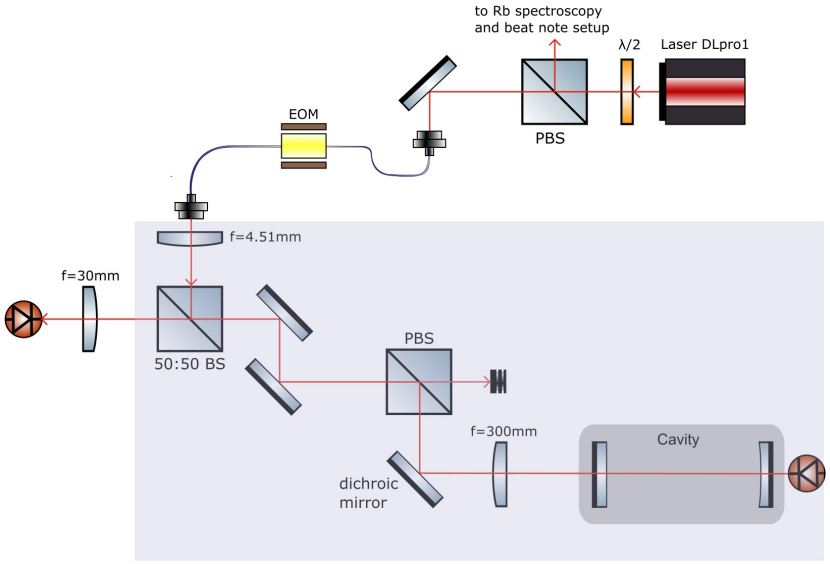

Figure 3.6: Optical setup for implementing the PDH method to stabilize the master laser to the cavity. The EOM modulates strong sidebands and sidebands for the PDH method onto the emitted laser light. The modulated light is coupled to the cavity and the reflected light is detected with the photodiode. The gray area describes the setup used for coupling to the cavity.

[6] Fiber EOM from EOSpace [43]

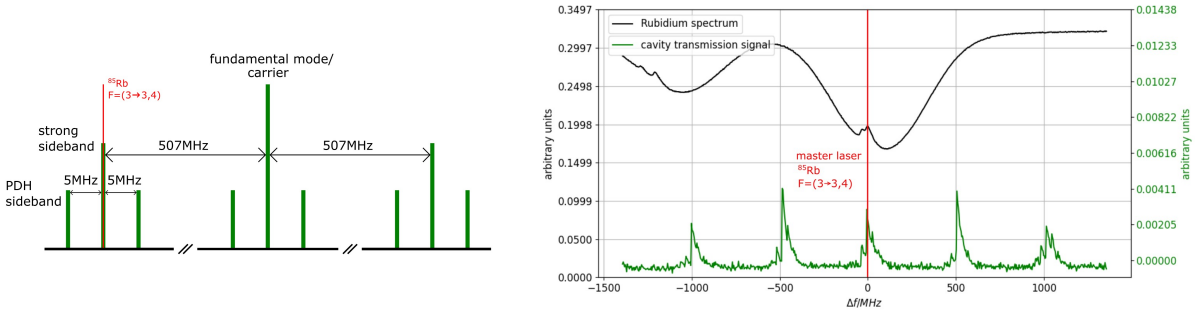

(a) (b)

Figure 3.7: **(a)** Schematic representation of the cavity transmission signal after modulation with the EOM. Strong sidebands are modulated at a frequency difference of ±507 MHz to the fundamental mode (carrier). In addition, PDH sidebands at 5 MHz are modulated to the strong sidebands. **(b)** Doppler-free saturation spectroscopy of rubidium and transmission signal after modulation with EOM. The strong sideband at the -1st order is shifted to the cross–over frequency. The PDH sidebands are not visible here.

3.1.1.4 Optical setup for locking the master laser

The optical setup for locking the master laser with the PDH method is shown in Fig. 3.6. The light that gets reflected at the PBS behind the master laser is used for the Rubidium spectroscopy and the frequency stabilization of the slave lasers. The transmitted light is coupled to a polarization maintaining fiber and is modulated by the EOM. A RF synthesizer[7] provides the strong sideband frequency. A mixer combines the PDH modulation signal from the local oscillator, with a modulation frequency of 5 MHz, with the strong sideband modulation signal. This new signal is then used as the modulation signal for the EOM. The cavity transmission signal after modulation with the EOM is shown in Fig. 3.7. For a more precise description of the electronics that are used for the modulation with the EOM see [25]. The output of the fiber then passes a 50 : 50 beam splitter (BS) and is coupled to the cavity. The reflected light from the cavity transmits through the 50 : 50 beam splitter and is detected on a photodiode.

3.1.1.5 Optimization of Master laser lock

The photodiode signal will be used to stabilize the master laser with a PID controller as shown in Fig. 3.4. The PID controller[8] with integrated low-pass filter and mixer generates the error signal. It consists of three integral parts (I), two differential parts (D) and one proportional part (P) called Gain. The P–part produces feedback proportional to the difference between setpoint and current value. The I–part integrates this difference over some adjustable time and reacts to slow changes. For compensating fast changes, the D–part can be used [46]. The output errorsignal produced by the PID can be fed back to the laser and controls the DC–modulation of the diode current and the scan offset to hold the laser at the desired frequency. The lock of the master laser is optimized by adjusting the parameters (I, D and Gain) of the PID controller while observing the error and transmission signal on an oscilloscope. For a good lock the cavity transmission signal should be maximized. To further optimize the lock, the error signal can be analyzed on a spectrum analyzer. The spectrum analyzer signal of the error signal, which

[7] SynthUSBII - USB RF Signal Generator from Windfreak Technologies [44]
[8] Fast Analog Linewidth Control FALC pro from TOPTICA [45]

Table 3.2: Optimized parameters for the PID controller when locking the master laser with the PDH method.

I_1	I_2	I_3	D_1	D_2	Gain
7.0 kHz	2.2 kHz	disabled	20 kHz	1.2 MHz	−7.0 dB

describes the distribution of the frequency components of the error signal, is shown in Fig. 3.8. The maximum of the signal is the so-called 'servo bump' that should be suppressed. The goal is to reduce the area under the signal and push the servo bump to high frequencies to achieve stable and fast locking properties. The found parameters for optimal locking conditions are given in Table 3.2.

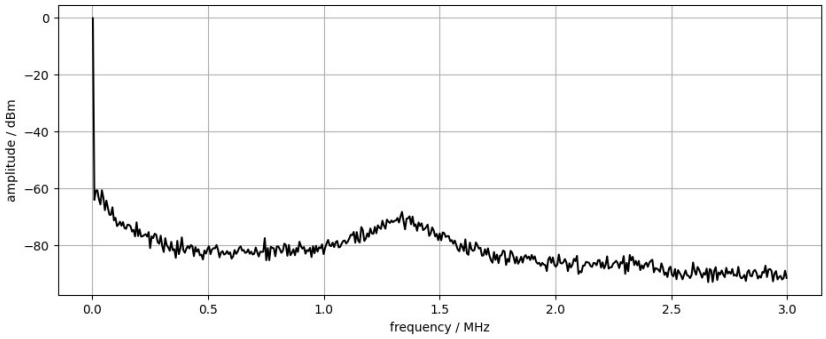

Figure 3.8: Error signal on spectrum analyzer. The maximum is the servo bump that should be suppressed and pushed to high frequencies for a stable lock.

3.1.2 Slave laser

The basic principle for locking the slave lasers relative to the master laser is to superimpose master and slave laser on a fast photodiode. The superposition of master and slave laser creates a beat note signal. Only the signal oscillating with $f_{\text{beat}} = f_m - f_s$, where f_m is the frequency of the master laser and f_s the frequency of a slave laser, can be detected with an AC coupled photodiode. The higher frequency terms are oscillating too fast and cannot be resolved with the photodiode. The aim is to hold the beat note frequency f_{beat} at a desired value what locks the slave laser to a frequency relative to the master laser frequency. This can be achieved with an optical phase-locked loop (OPLL). This is a feedback control system that phase-locks a slave laser with a variable scan offset to the master laser [47]. The beat note signal is then sent to a PLL board[9] , which is integrated in the beat note box that was built by Julia Gamper [25], where it gets compared to a RF frequency reference signal defined by $f_{\text{ref}}/2 = f_{\text{beat}}/N (= 8, 16, 31, 64)$ [49]. The error signal which depends on whether the frequency of the signal is greater or lower than the reference is fed back to the slave laser with a homemade PI-controller. The output of the controller will be used to adjust the diode current of the slave laser to stabilize the beat note frequency at the desired frequency.

The frequency difference between transition frequency of the master laser and the transition for cooler and repumper light is given in Table 3.3. Since the cooling and repumping light passes an AOM before they are aligned in the MOT (see Section 3.2.1), their frequencies will be shifted around 80 MHz. So the

[9] ADF4007 High Frequency Divider/PLL Synthesizer von Analog Devices [48]

Table 3.3: Frequency difference between transition frequency of master laser and required transition frequency of cooler and repumper light. Because of the 80 MHz frequency shift due to the AOM, the actual desired beat note frequency f_{beat} differs from the frequency difference of the transitions. Furthermore, the cooler laser should be red detuned about δ.

	transition frequency difference	f_{beat}
cooler	$-1\,066\,\text{MHz} - \delta$	$-1\,146\,\text{MHz} - \delta$
repumper	5 501 MHz	5 421 MHz

beat note frequency is shifted as well 80 MHz relative to the actual frequency difference of the transitions. In addition to that the cooler light should be red detuned about δ.

The optical setup for locking cooler and repumper relative to the master laser is shown in Fig. 3.9. For the locking process of the cooler laser the side output of the TApro1 laser is used. The PBS and $\lambda/2$-plates behind the output of the master laser split the incident laser beam in different beams with variable power to use the light for the Rb-spectroscopy, the PDH locking and the locking of the slave lasers at the same time. With the help of a beam sampler some light gets directed to a wavemeter[10] . For the cooler and repumper laser a 50 : 50 beam splitter (BS) is used instead of a beam sampler, due to lower power of the laser beams. The wavemeter measures the wavelengths of the lasers with a resolution of 200 MHz and is used to adjust the frequency of the lasers before locking to make sure that the beat notes are approximately at the right frequencies. The light of cooler and repumper laser that gets transmitted

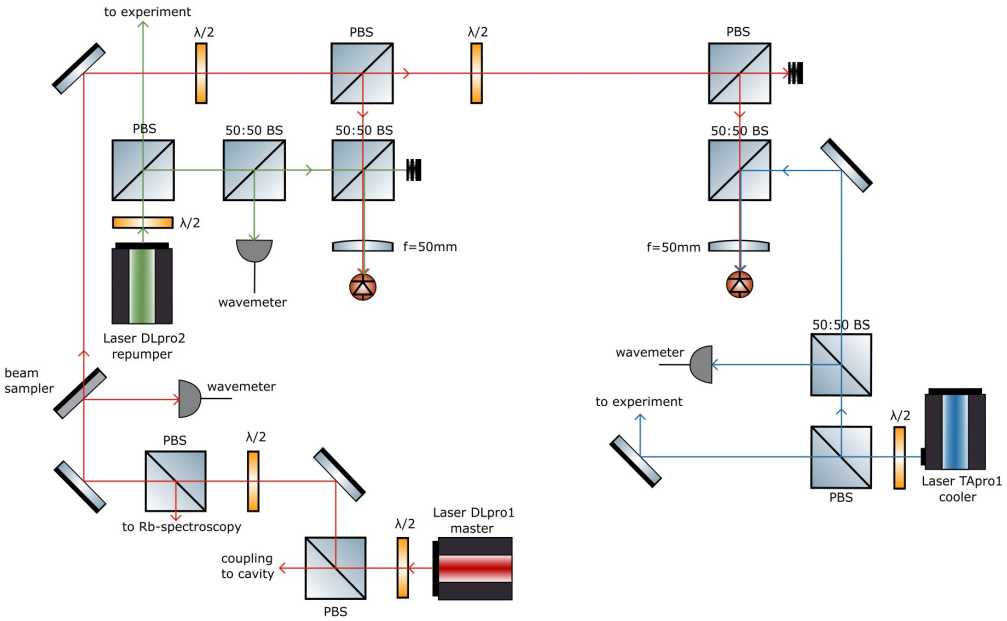

Figure 3.9: Optical setup for locking cooler and repumper laser to the master laser with an optical phase locked loop. Master and slave lasers are superimposed at a 50 : 50 BS. The beat note signal is detected with a photodiode and will be processed with the PLL board.

[10] WS6-200 Series High Precision Wavemeter from HighFinesse [37]

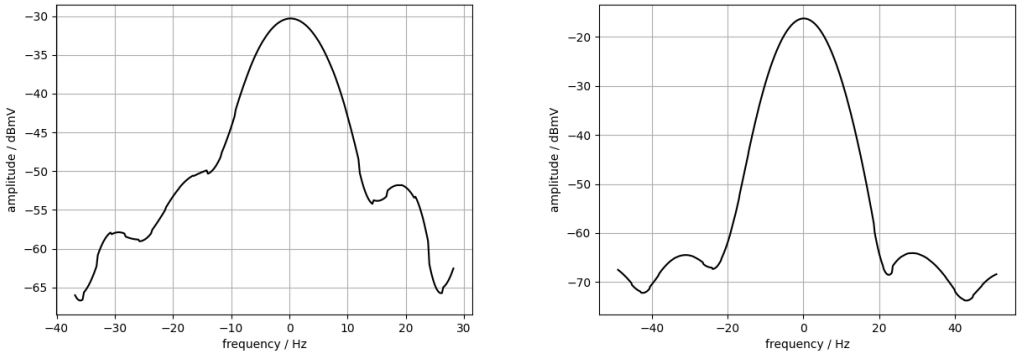

Figure 3.10: Frequency spectrum of the beat note of the master laser with DLpro2 (left) and TApro1 (right). The signals are centered around zero. For both lasers a beat note signals with a linewidth of around 20 Hz was reached.

through the first 50 : 50 beam splitter is superimposed with the master laser at a second 50 : 50 beam splitter and detected at a fast photodiode[11] to create the beat note. The in the beat note box amplified beat note signal can be observed on a spectrum analyzer and the output error signal of the PI controller, that will be fed back to the slave lasers, can be observed with an oscilloscope. The P and I value will be adjusted in such a way that the amplitude of the error signal and the linewidth of the beat note signal on the spectrum analyzer are as small as possible. The goal is to achieve a linewidth of the beat note signals that is equal to or less than the natural linewidth of the transition [25] of 6 MHz [22]. As can be seen in Fig. 3.10 a linewidth of around 20 Hz was reached for both cooler (TApro1) and repumper (DLpro2) laser. The measured linewidth, limited by the 10 Hz resolution of the spectrum analyzer, is clearly below the linewidth of the transition what characterizes the OPLL as a good method to stabilize a slave laser onto a master laser and to use those as repumper and cooler laser for a MOT. The beat note is only a measure for the frequency stabilization of the slave lasers relative to the master laser. So the stabilization and thus the linewidth of the slave lasers is limited by the linewidth of the master laser. An upper limit for the linewidth of the master laser of 1.3 kHz was estimated by Florian Pausewang [51].

3.2 Light distribution

After the cooler and repumper light is stabilized in frequency it has to be guided to the vacuum chamber and split into the six MOT beams which is done with fiber beam splitters. Furthermore, acousto-optical modulators (AOM) that act as a switch for the MOT beams and can control the power of the light are integrated in the laser system.

3.2.1 Acousto-optical modulator (AOM)

An acousto-optical modulator (AOM) consists of a crystal and a piezoelectric transducer driven by an RF source to create sound waves in the optical medium [52]. Light passing through the AOM gets diffracted due to periodic fluctuations of the refractive index induced by the sound waves. This produces several beams at the output, characterized by the order m, the diffraction angle θ_m and with

[11] Ultrafast MSM photodetector G4176-03 from Hamamatsu [50]

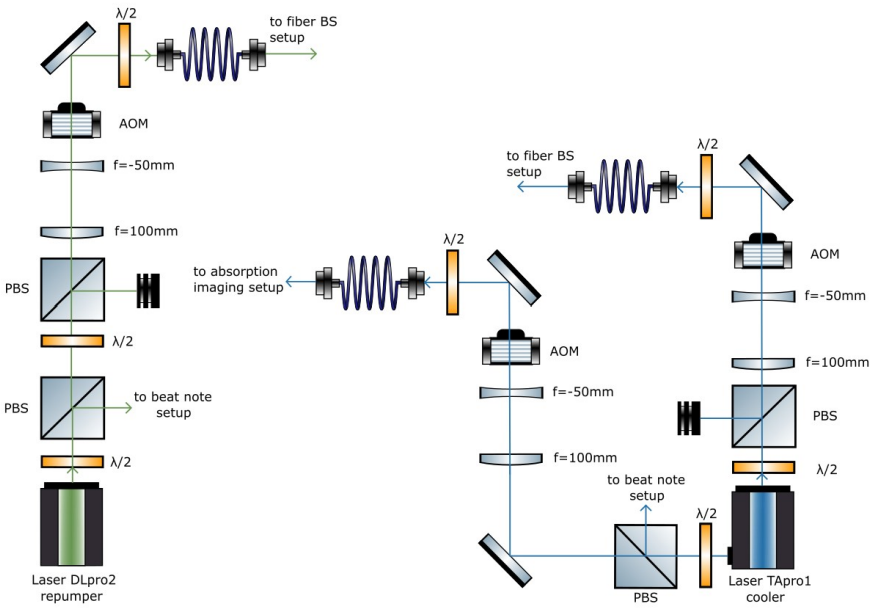

Figure 3.11: AOM setup for switching the laser light in the MOT on and off. The telescopes in front of the AOM adjust the beam size to the size of the active aperture of the AOM. The $+1^{st}$ order of the diffracted beam is coupled to the polarization maintaining fibers. When turning the RF signal for the AOM off, the $+1^{st}$ order vanishes and no light will reach the fiber output

a frequency of $f + mf_s$ where f is the frequency of the incident light and f_s is the frequency of the sound waves [52]. Furthermore, the intensities of the diffracted beams depend on the power of the sound waves [53]. Therefore, by adjusting the amplitude of the RF signal, the intensity of the diffracted beam can be controlled. The RF signal with an adjustable frequency and amplitude is generated by a homebuilt frequency source. This box consists of a direct digital synthesizer (DDS) chip that provides an output signal between 40 MHz and 200 MHz. The output of the DDS board will be attenuated by a RF mixer that mixes the RF signal with an adjustable DC signal (0 V − 10 V) to control its intensity. After that the attenuated RF signal is guided to a RF switch. A TTL can control if the signal passes the switch or not. If the signal gets transmitted, it will be amplified before reaching the output of the AOM box.

The implemented optical setup is shown in Fig. 3.11. Three acousto-optical modulators[12] are placed in the beam path of the DLpro2 laser and of the side and main output of the TApro1 laser. The telescopes in front of the AOMs are used to adjust the size of the beams to the size of the active aperture of the AOMs defined by the crystal size. If the size of the incident beam is smaller than the active aperture, the response time of the AOM is higher, but there are losses in efficiency. For the setup it is more important to have a high efficiency than a fast response time. In the HQO setup around 70% − 86% of the total power behind the AOMs could be aligned into the $+1^{st}$ order. This corresponds to the expected diffraction efficiency of the used AOMs [54]. The $+1^{st}$ order of all AOMs is coupled to polarization maintaining fibers (PMF) that guide the light to the vacuum chamber. By turning the AOM off the $+1^{st}$ order vanishes and no light passes through the fiber. To make sure that even if some light still leaks into the first order no light is coupled to the fiber when the AOM is turned off, optical shutters will be placed behind the

[12] Gooch & Housego AOMO 3080-122 [54]

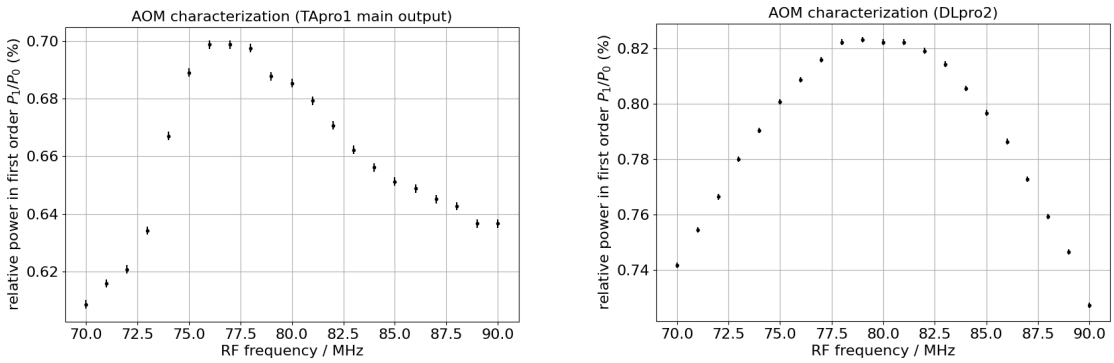

Figure 3.12: AOM characterization for cooler and repumper AOM. The maximum of the relative power is between 76 MHz and 77 MHz for the TApro1 AOM and at 79 MHz for the DLpro2 AOM.

AOM in the future. The $\lambda/2$–plates in front of the polarization maintaining fibers are used to align the polarization axis of the input light with one of the polarization maintaining fiber axes. The light of the side output of TApro1 that is coupled to the fiber after passing the AOM will be used for absorption imaging (see Section 4.2). The light of DLpro2 and the main output of TApro1 will be guided with a PMF to the fiber beam splitter setup (see Section 3.2.2) and will be used as repumper and cooler light.

The operating frequency of the used AOM[13] is 80 MHz [54]. To verify this, the RF frequency was varied from 70 MHz to 90 MHz and the power P_1 in the $+1^{\text{st}}$ order compared to the total power P_0 behind the AOM was measured. The characterization was carried out for the cooler and repumper AOM. In Fig. 3.12 the relative power P_1/P_0 is plotted against the applied RF frequency. For the AOM in the TApro1 beam path the maximum of the relative power is between 76 MHz and 77 MHz. For the AOM in the DLpro2 beam path the maximum is at 79 MHz and the measured values around the maximum are more evenly distributed. Since the maxima are near 80 MHz and the relative power at 80 MHz is still high enough, all AOMs are driven with a RF signal of 80 MHz for the scale of simplicity.

3.2.2 Fiber beam splitter

The distribution of cooler and repumper light along the six MOT axes can be done with fiber beam splitter. To adjust the power of the MOT beams on the horizontal and vertical axis independent of each other a 2x2 fiber beam splitter and a 2x4 fiber beam splitter is used. A fiber beam splitter has two input ports for two different light sources, and in this case two or four output ports. The fiber beam splitter splits both input fields evenly in two or four parts and mixes both fields. That is how every output provides light from both input sources.

The setup for coupling into the fiber beam splitters is shown in Fig. 3.13. The PBS behind the fiber output is used to clean the polarization of the light. The beam sampler reflects a small amount of light to the photodiode. This signal will be used for intensity stabilization in the future. The second PBS and $\lambda/2$–plate split the incoming light in two beams with adjustable splitting ratio. These two beams are coupled to the 2x2 and 2x4 fiber beam splitters.[14] The output of the 2x2 fiber BS (X,Y) will be used for the two vertical MOT beams, and the output of the 2x4 fiber BS (1,2,3,4) for the horizontal MOT beams.

[13] AOMO 3080-122 from Gooch&Housego [54]

[14] 2x4 and 2x2 polarization maintaining fiber beam splitter from Evanescent optics [55]

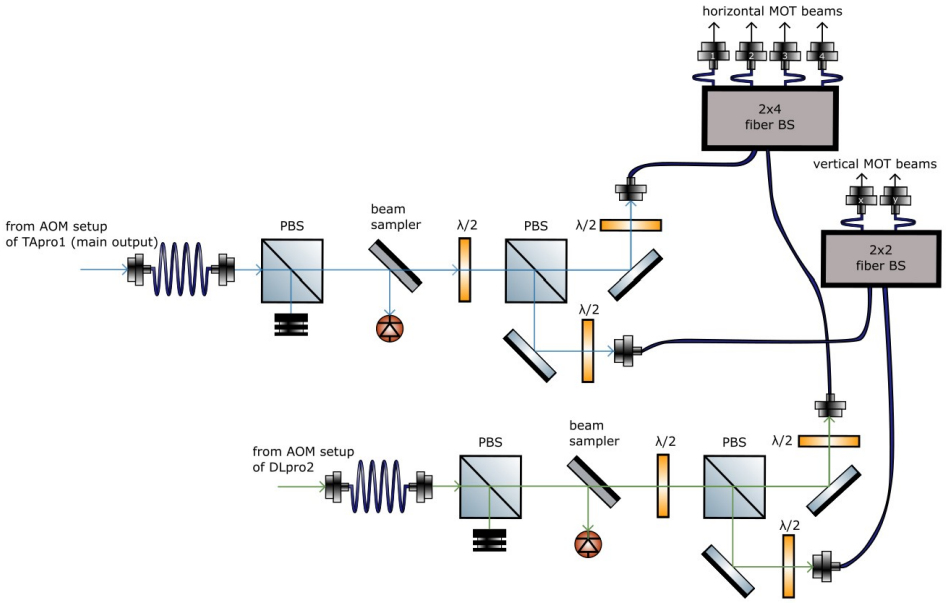

Figure 3.13: The light behind the AOM is guided through a polarization maintaining fiber to the fiber beam splitter setup. The 2x4 fiber BS is used for the horizontal MOT beams and the 2x2 fiber BS for the vertical MOT beams.

CHAPTER 4

Realization and imaging of a magneto-optical trap

After the laser system including frequency stabilization and light distribution was built, the MOT could be realized. For optimizing the cooling process, it is important to find out about the number of atoms that are trapped, the atomic density and the temperature of the atom cloud. This can be done for example with fluorescence imaging or absorption imaging. As part of this thesis an absorption imaging of the HQO MOT was built to characterize the MOT. Due to a delay in the delivery of one fiber beam splitter the MOT was only realized about a week before the end of this thesis which is why the absorption images could not be evaluated and the MOT parameters could not be optimized anymore. However, a characterization of the imaging system was carried out.

4.1 Absorption imaging

The basic principle of absorption imaging is to illuminate the cold atom cloud with a resonant collimated laser beam and detect the transmitted light with a camera behind the cloud, creating an image of the shadow of the atom cloud. This shadow describes the spatial distribution of the cloud [16]. In order to derive the column density $n_{\mathrm{a}}(x, y)$ from the absorption images, a two level atom is considered. The following derivation is based on [16]. When the light passes through the atom cloud, it gets absorbed and diffracted. The real part of the complex refractive index $n = n' + in''$ describes the diffraction and is zero for resonant light and the imaginary part n'' describes the absorption of the light [53, 56]. Since the complex refractive index can be expressed in terms of the optical susceptibility χ the electric field after passing through the atom cloud can be described as [16]

$$\vec{E} = \frac{E_0}{2}\vec{\epsilon}\left[e^{-i(\omega t - k\int n\, dz)} + e^{i(\omega t - k\int n^*\, dz)}\right] = \frac{E_0}{2}\vec{\epsilon}e^{-k/2\int Im(\chi)\, dz}\left[e^{-i(\omega t - kl)} + e^{i(\omega t - kl)}\right],$$

where E_0 describes the amplitude of the electric field, $\vec{\epsilon}$ is the normalized polarization vector, ω is the frequency of the imaging light, k the wave number, z the propagation axis and l the propagation distance.

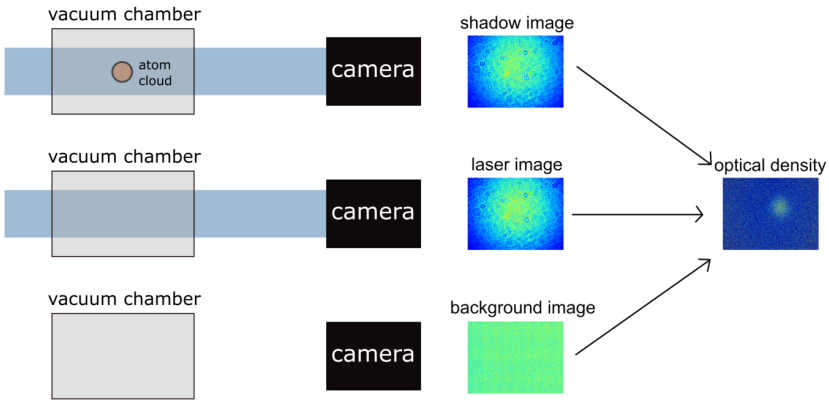

Figure 4.1: Measuring principle for absorption imaging. Three images have to be taken, one image while illuminating the atoms (shadow image), the second image is an image of only the imaging beam and the third image is taken without atoms and imaging light (background image). Image modeled after [16].

The transmission $T(x, y)$, determined by the intensity I in front of and behind the atom cloud is given by

$$T(x,y) = \frac{I(x,y,z=l)}{I(x,y,z=0)} = \exp\left[-k\int_0^l Im(\chi)dz\right] = \exp\left[-\sigma\int_0^l n_a(x,y,z)dz\right].$$

This leads to a cross section defined as $\sigma = \frac{\sigma_0}{1+(\frac{2\delta}{\Gamma})^2+I/I_{sat}}$ where σ_0 is the resonant cross section for low intensity, δ is the detuning and Γ the atomic linewidth. The intensity of the light behind the cloud follows Beer's law, which can be used to derive the column density $n_a(x, y)$. For resonant light and low intensity follows

$$n_a(x,y) = \int_0^l n_a(x,y,z)\,dz = -\frac{1}{\sigma_0}\ln\frac{I(x,y,z=l)}{I(x,y,z=0)} = \frac{1}{\sigma_0}od(x,y),$$

where $od(x,y) = -\ln\frac{I(x,y,z=l)}{I(x,y,z=0)}$ is the optical density [16].

In the actual experiment three images must be taken for measuring the optical density. The first image is the shadow image $S(x, y)$ where the atoms are illuminated by the imaging beam. Then a second picture of the imaging beam without any atoms in its path is taken to get the intensity profile of the laser light $L(x, y)$. The third picture is a picture without light and without atoms in the MOT and provides the background signal $B(x, y)$. This principle of measurement is illustrated in Fig. 4.1. With these images the optical density can be determined by

$$od(x,y) = -\ln\frac{I(x,y,z=l)}{I(x,y,z=0)} = -\ln\frac{S(x,y)-B(x,y)}{L(x,y)-B(x,y)}. \tag{4.1}$$

Besides the density, the atom number can be obtained by integrating $n_a(x, y)$ along the x– and y–direction [57]. Furthermore, the determination of the optical density at different times t after releasing the atoms from the trap allows it to measure the temperature of the atoms. The principle of this time of flight (TOF) measurement is explained in Appendix A.3.

4.2 Imaging setup

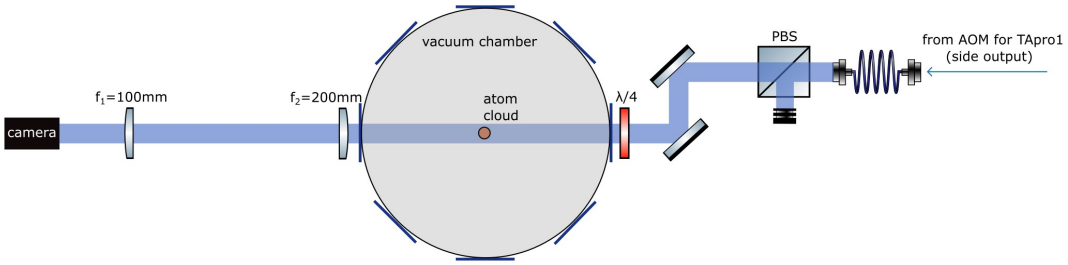

Figure 4.2: Optical setup for absorption imaging. The fiber output gets circularly polarized and passes through the atom cloud in the vacuum chamber. The light is then imaged onto the camera.

The optical setup for the absorption imaging is shown in Fig. 4.2. The light behind the AOM for the side output of TApro1 (see Section 3.2.1) is guided by a polarization maintaining fiber to the experiment. A lens ($f = 100\,\mathrm{mm}$) behind the fiber output collimates the beam and determines a $1/e^2$ beam diameter of 18 mm. The imaging happens on the cooling transition $[5S_{1/2}(F = 2, m_F = 2) \rightarrow 5P_{3/2}(F = 3, m_F = 3)]$ of ^{87}Rb. So the light has to be circularly polarized which can be achieved with the $\lambda/4$–plate in the beam path. To be able to drive the $\Delta m_F = +1$ transition compensation coils will be mounted around the chamber to define a quantization axis. Since the diameter of the whole MOT is greater than the resolution of the CCD camera[1] , an imaging system with a magnification of $1/2$ realized by two achromatic lenses ($f_1 = 100\,\mathrm{mm}$[2] , $f_2 = 200\,\mathrm{mm}$[3]) was built behind the chamber what is shown in Fig. 4.3.

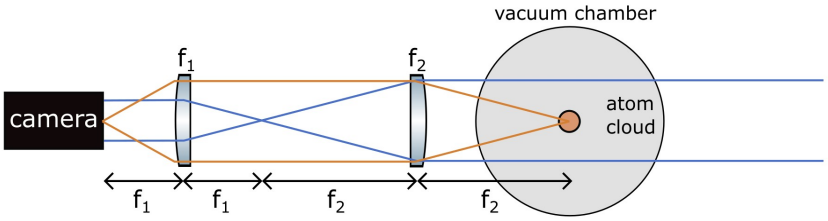

Figure 4.3: Imaging system for absorption imaging. The orange lines describe the image of the atom cloud and the blue lines the imaging light. The first lens is placed at a distance of $f_1 = 100\,\mathrm{mm}$ to the camera, the second lens is placed at a distance of $f_2 = 200\,\mathrm{mm}$ to the atom cloud. The distance of the lenses is $f_1 + f_2$.

4.3 Image acquisition

The image acquisition in the HQO experiment can be controlled by the experiment control system [61]. The experiment control GUI can be used to progress analog and digital voltage sequences which control the different devices of the experiment. The voltage sequences are transferred to the ADwin-Pro II, which has 16 analog and 32 digital output channels that generate trigger pulses for the devices. The

[1] pco.pixelfly usb CCD camera [58]
[2] AC508-100-B from Thorlabs [59]
[3] AC508-200-B from Thorlabs [60]

variables for the 16 channel USB analog voltage source (USB MCC DAQ), that provides controllable voltage signals which, however, cannot be changed during one sequence, can also be defined in the experiment control GUI [61]. To take absorption images of the atom cloud in the MOT, an imaging sequence has to be implemented (see Fig. 4.4) in the experiment control GUI. The green lines in Fig. 4.4 show if the device is turned on (high) or off (low). To realize this sequence the cooler, repumper and imaging light have to be controlled by switching the corresponding AOM and shutter on and off. The shutters are not yet integrated in the current setup, but they are already considered here. What is not shown are the analog outputs that control the detuning and intensity of the cooler and repumper and the

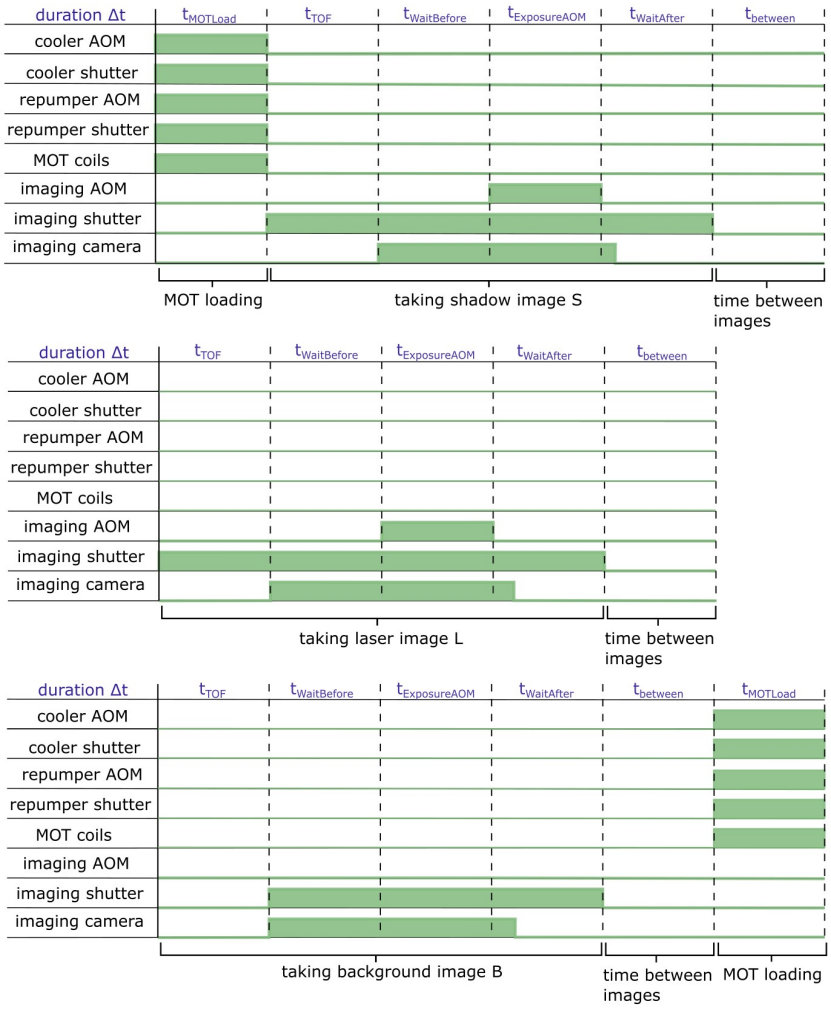

Figure 4.4: Implemented sequence in experiment control GUI for the image acquisition. This is one sequence that will be repeated for the number of scans. At first the MOT will be loaded. Then the MOT is turned off and the shadow image, the laser image and the background image are taken. At the end of the sequence the MOT will be loaded again. The green lines show if the device is turned on (high) or off (low). The exposure time of the camera is set to 100 µs. For the first test runs, when the dispenser was not turned on yet, the following time periods were used: $t_{\mathrm{MOTLoad}} = 200\,\mathrm{ms}$, $t_{\mathrm{TOF}} = 5\,\mathrm{ms}$, $t_{\mathrm{WaitBefore}} = 0.02\,\mathrm{ms}$, $t_{\mathrm{ExposureAOM}} = 0.06\,\mathrm{ms}$, $t_{\mathrm{WaitAfter}} = 0.1\,\mathrm{ms}$, $t_{\mathrm{between}} = 100\,\mathrm{ms}$.

current of the MOT coils. The sequence consists at first of a MOT loading phase where the cooler and repumper beam (controlled by the AOM and shutter) and the MOT coils are turned on. For the imaging the MOT has to be turned off again. After that the three pictures, the shadow image, the laser image and the background image, will be taken. When this is done, the MOT will be turned on again. The camera is not turned on immediately after turning off the MOT. During a time of flight t_{TOF} the cloud can thermally expand. Since the shutter has a reaction time of $\sim$ ms it is already switched on during the expansion time. The exposure time of the camera is set to 100 µs. The time the imaging light illuminates the atoms is shorter than the exposure time of the camera, so that all of the light will be detected. After a waiting time t_{between} the laser image will be taken in the same way as the shadow image, only that the MOT is not loaded again so that there are no atoms in the beam path. For the last image the imaging AOM will stay off to only detect the background. At the end the MOT loading process starts again, so that this sequence can be executed all over again.

The images are saved on the experimental central data server. The additional information about the sequence that was used for acquiring the images, like e.g. the starting global counter that identifies a run, the specific global counter for an image, the scan variables and number of iteration, is saved to a MySQL database [61].

4.4 Characterization of the imaging setup

Before imaging cold atoms in the MOT, the imaging setup is characterized without trapped atoms. The following provides the results of a power stability test and of a test for the stability of the optical density when no atoms are trapped in the MOT.

4.4.1 Power stability test

To test the stability of the imaging power a test run with the image acquisition sequence shown in Fig. 4.4 is performed. The power of the imaging beam will be scanned by changing the voltage applied to the AOM RF-signal generator (see Section 3.2.1). The voltage will be increased from 1.5 V to 8 V with a step size of 0.5 V. At the end the imaging power P_{Img} behind the vacuum chamber for each applied voltage was measured with a powermeter. To check the stability of the imaging power a test run with 1148 scans was done overnight.

The CCD camera produces electronic charge proportional to the incident light intensity [53]. Thus, the total number of counts on the CCD camera, obtained by summing over the counts for every pixel, corresponds to the total power of the imaging light that was detected with the camera. The left images in Fig. 4.5 show the number of total counts for the different imaging powers P_{Img} and for every scan. Since the imaging power for the last three voltage values did not increase anymore due to a saturation of the AOM and the power fluctuations of the AOM output are stronger for higher RF power, the total counts for the last three scan values are not shown here for the sake of clarity. In the right images the total counts for one random scan are shown. As expected, the results for the shadow image and the laser image look the same, since both pictures are taken without atoms present. The number of total counts stays almost constant over 1148 scans. There are still some small fluctuations in the order of 1% – 2% that are probably caused by polarization fluctuations induced by the fiber. Because a PBS is placed behind the polarization maintaining fiber, a polarization fluctuation results in a fluctuation of the intensity. These polarization fluctuations can occur due to stress applied to the fiber and a change of

temperature. Since the fluctuations are on time scales that a greater than the time period of on sequences they will have no influence on the single absorption images[4] . Background noise and stray light are the reason for the non-zero background signal shown in Fig. 4.5.

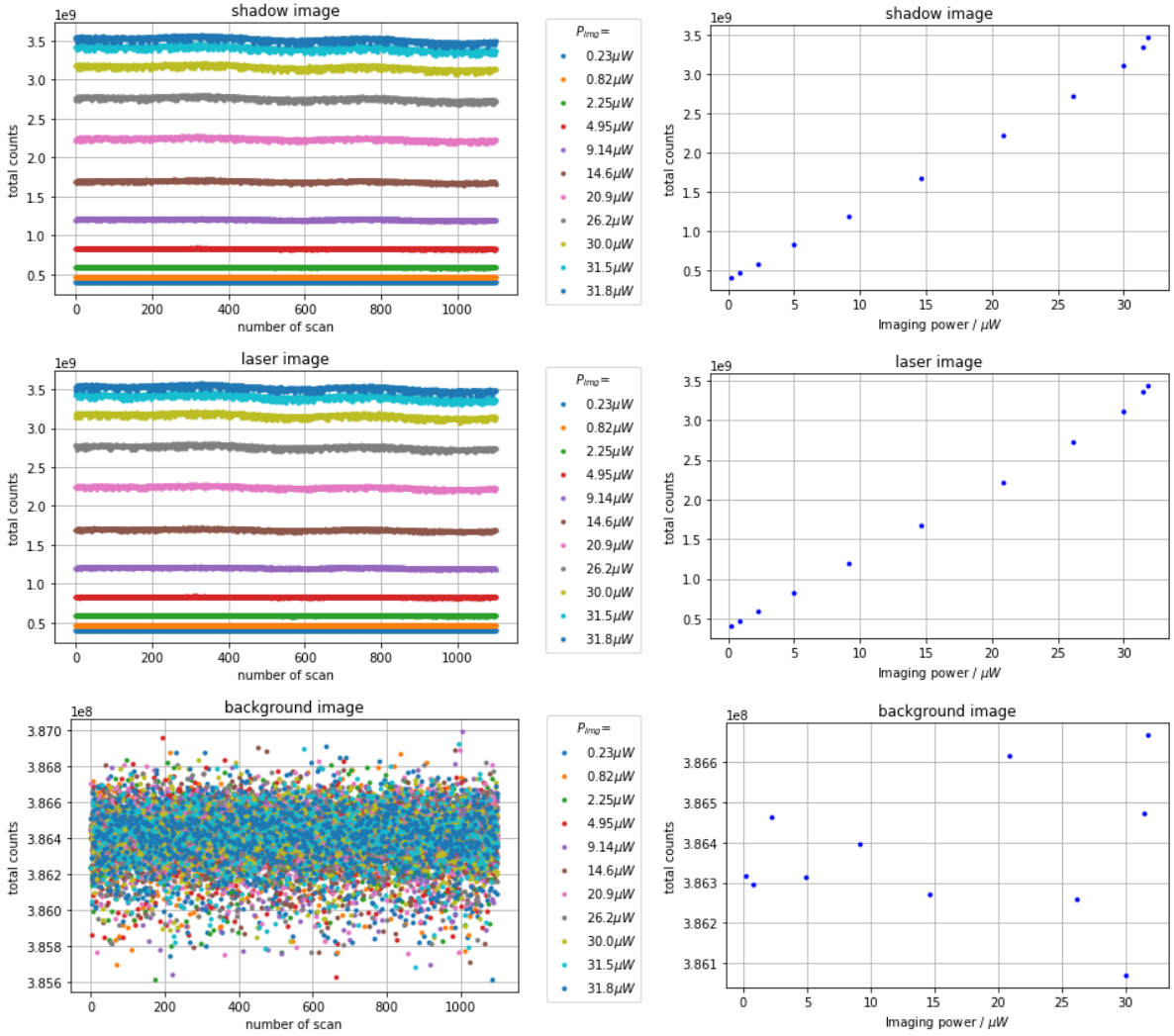

Figure 4.5: Results from the power stability test. The total counts, generated by the CCD camera when the light is detected, is plotted against the number of the current scan (left) and the total counts for one specific scan is shown on the right. P_{Img} is the power of the imaging light.

[4]Due to initially not explainable fluctuations in the signals when the power stability test was carried out for the first time, we found out that the trigger boxes for the pixelfly cameras are specified for the cameras. If the camera is connected to the wrong trigger box, there is a delay in the trigger pulse that causes fluctuations.

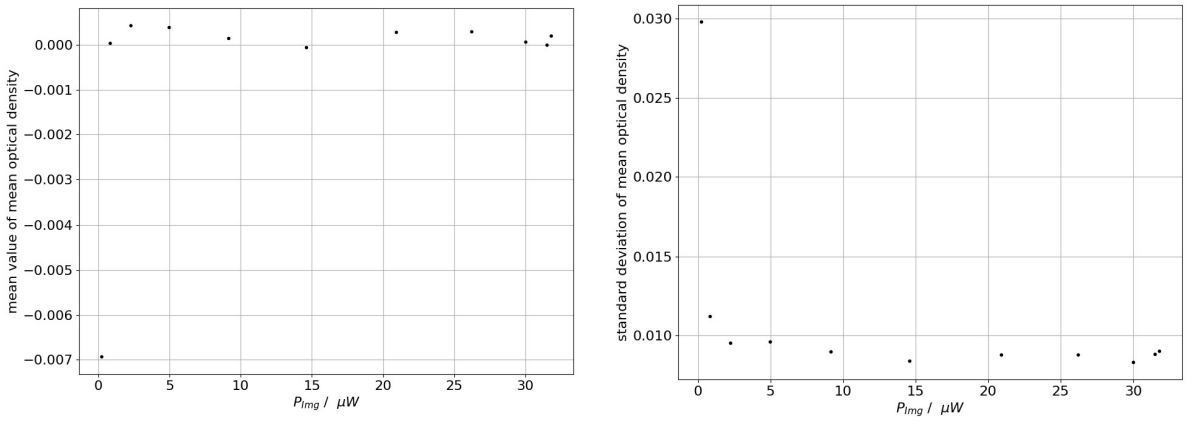

(a) (b)

Figure 4.6: **(a)** The mean value of the mean optical density of all sequences that have been run through in the test run is plotted against the imaging power P_{Img}. The mean optical density is centered around zero since no atoms were trapped in the MOT during the test run. **(b)** Standard deviation of the mean optical density for every imaging power. Due to a low signal–to–noise ratio the standard deviation of the lowest imaging power is relatively high.

4.4.1.1 Stability of optical density

The optical density is used to describe the transmission through an atom cloud and is proportional to the column density of the cloud. When no atoms are in the path of the imaging light, the optical density is expected to be zero. A strong deviation from zero of the optical density with no atoms trapped, would indicate intensity fluctuations on time scales in the order of the time between shadow and laser image. The optical density, for the images that were taken during the test run, can be calculated with Eq. (4.1). For every sequence one can calculate a mean optical density by averaging over the two-dimensional optical density distribution. Fig. 4.6(a) shows the mean value of the mean optical densities calculated for every sequence of each scan variable, plotted against the power of the imaging beam P_{Img} with the standard error as error bars. Since the standard error is proportional to $1/\sqrt{N}$, with N being the number of samples, and here $N = 1148$ scans were run through, it is relatively low, and the error bars are not visible in the plot. In Fig. 4.6(b) the standard deviation of the mean value of the mean optical density is plotted against the imaging power.

The mean value of the mean od is around zero for every imaging power which indicates that there are no short term intensity fluctuations of the imaging beam. Only for an imaging power of $(0.23 \pm 0.02)\mu\text{W}$ the mean value is slightly smaller than zero. An $od < 0$ means that for the first picture more charge was generated on the CCD camera than for the second. The reason for this could be that before the shadow picture is taken, charge produced by stray light is collect on the CCD, but between laser and background picture there is less time during which stray light can produce additional charge. This affects the measurement for low imaging power more strongly since the signal–to–noise ratio is lower. The low signal–to–noise ratio also causes a higher standard deviation for low power (see Fig. 4.6(b)). For the second measurement with an imaging power of $(0.82 \pm 0.02)\mu\text{W}$ the standard deviation is already much lower, so for absorption imaging an imaging power higher than this should be used.

4.5 First realization and imaging of the MOT

When trying to realize a magneto-optical trap the fluorescence image can be used as a first indicator whether atoms are trapped or not. The fluorescence image for the first successful attempt of trapping rubidium atoms in the HQO magneto-optical trap is shown in Fig. 4.7. The bright point in the picture shows the atom cloud.

Fig. 4.8 shows the absorption image that was taken after the MOT was successfully realized for the first time. Since the absorption imaging parameters, like for example imaging time and imaging power, are not optimized and the compensation coils are not yet installed, so no quantization axis is defined, the absorption image is still pretty noisy, and the noise is of the order of the signal. Nevertheless, the images show that it was possible to trap and cool down ^{87}Rb atoms in the MOT.

Figure 4.7: The picture shows the fluorescence image for the first successful attempt of trapping rubidium atoms in the HQO MOT. The following parameters were used: detuning cooler laser: -11 MHz; dispenser current: 5.07 A; magnetic field gradient: 18 G/cm; MOT loading time: 10 s, peak intensity cooler light: $8.7\mathrm{mW/cm^2}$ (horizontal), $8.5\mathrm{mW/cm^2}$ (vertical) ; peak intensity repumper light: $0.2\mathrm{mW/cm^2}$ (horizontal / vertical); pressure in vacuum chamber: $1.1 \cdot 10^{-9}$mbar.

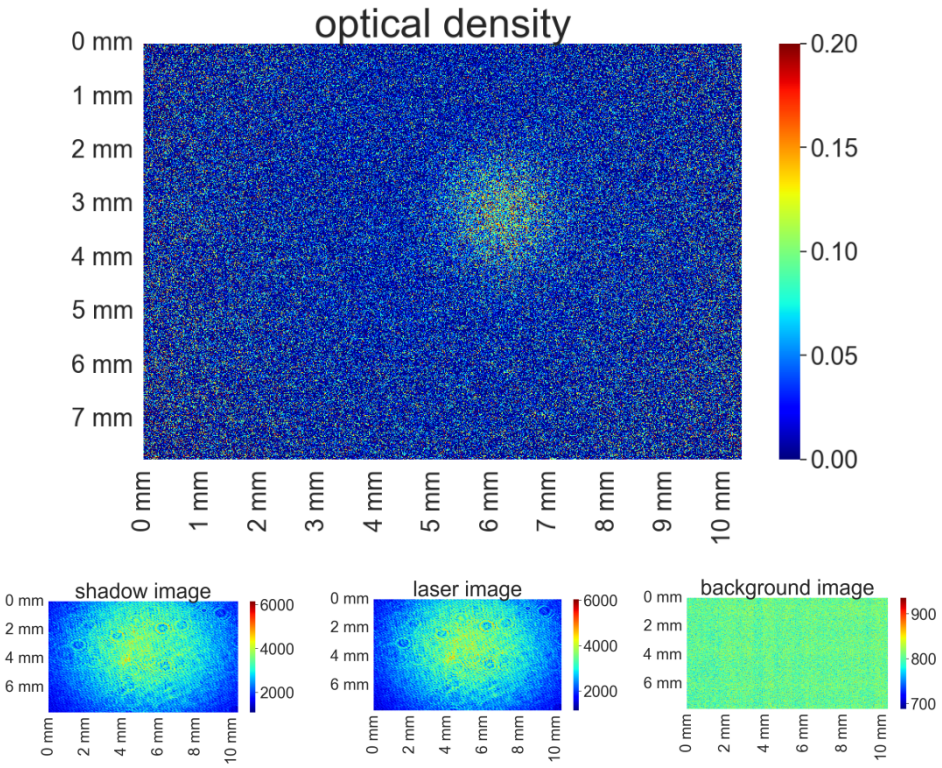

Figure 4.8: Absorption image for first MOT realization. At the bottom the shadow image, the laser image and the background image can be seen. The color scale for these three images describes the counts per pixel. With these images the actual absorption image can be determined which is shown in the picture on top. The optical density is represented by the color scale on the right. For the scale on the x– and y–axis the magnification with a factor of 2 due to the imaging system is already considered.

CHAPTER 5

Conclusion

The aim of this thesis was to realize a MOT for the HQO experiment as the first cooling step. After the rubidium atoms are initially cooled down and trapped in the MOT, they will be transported via a magnetic transport to the cryogenic science chamber. Therefore, the MOT is an important part for realizing the two-chamber system in the experiment.

The first step for realizing a MOT was to set up the laser system so that the two lasers TApro1 and DLpro2 can be used as cooler and repumper laser. At first a third master laser was locked to a reference cavity with the Pound–Drever–Hall (PDH) method. The lock was optimized by analyzing the frequency components of the error signal and adjusting the parameters of the PID controller. The slave lasers could then be stabilized relative to the master laser by using an optical phase–locked loop. After optimizing the lock parameters, the beat note signal of the master laser with each slave laser (TApro1, DLpro2) reached a linewidth of around 20 Hz. This is even better than necessary for realizing a MOT since the linewidth of the beat note signal is smaller than the natural linewidth of the cooler and repumper transition of 6 MHz. However, the beat note only characterizes the stabilization of the slave lasers relative to the master laser. Furthermore, three AOMs, that act as a switch for the MOT beams and can control the power of the beams during different cooling phases, were integrated in the laser system and two of them were characterized. The next step would be here to place shutters behind the AOMs. Since there still can be some leakage in the first order when the AOM is turned off, the shutter can block this light to make sure that no light passes through the vacuum chamber. After building the AOM setup the repumper and cooler light were coupled to fiber beam splitters to distribute the light along the six MOT axes. Unfortunately, there was a delay in the delivery of one fiber beam splitter what slowed down the process of realizing the MOT. Because of this the MOT was only ready to trap and cool atoms about a week before the end of this thesis and no further characterization and optimization was carried out.

So, before the realization of the MOT, the absorption imaging setup for the MOT was built and characterized without trapped atoms. A test for the stability of the imaging light power and of the optical density was carried out. The results showed that there are long-term drifts of the polarization that induce fluctuations in the power in the order of $1\% - 2\%$ which is acceptable for the imaging. Since the fluctuations are on time scales that are greater than the time period of the single sequences, they will not influence the single absorption images and the calculation of the optical density.

Nevertheless, a next step will be to integrate an intensity stabilization system for the MOT beams into to the current setup to achieve long-term stabilization. The optics for doing this are already in place, but

the PID controllers still have to be connected with the photodiode signal for realizing a feedback loop.

In this thesis it was possible to realize the ^{87}Rb magneto-optical trap and first fluorescence and absorption images could be taken. A next step will be to determine the number of trapped atoms and the temperature of the atom cloud with the help of the absorption images. For this the compensation coils have to be mounted on the vacuum chamber to define a quantization axis when the MOT coils are turned off for the imaging to have a well-known scattering rate. Furthermore, the operating parameters of the MOT must be optimized to increase the trapping rates and decrease the temperature of the atom cloud. This can be done by adjusting the detuning and power of the cooler laser, the power of the repumper laser, the gradient of the magnetic field generated by the MOT coils and the dispenser current. After this the magnetic trapping in a strong quadrupole field will be realized by the MOT coils, as a first step for the magnetic transport into the science chamber.

Appendix

APPENDIX A

Appendix

A.1 Mode matching

The fundamental transverse TEM_{00} mode describes a Gaussian beam. The intensity of the beam in the transverse plane is Gaussian distributed. The beam is characterized by the width $w(z)$ that denotes the distance to the propagating axis where the intensity is equal to $1/e^2$ of the maximal intensity. The width evolves along the propagation axis according to [40]

$$w(z) = w_0\sqrt{1 + \left(\frac{z}{z_R}\right)^2}$$

where z is the distance along the propagation axis, w_0 is the minimal beam size called beam waist, $z_R = z\left(w = \sqrt{2}w_0\right) = \frac{\pi w_0^2}{\lambda}$ is the Rayleigh range and λ the wavelength of the light. The radius of curvature of the wavefront is given by [40]

$$R(z) = z\left[1 + \left(\frac{z_R}{z}\right)^2\right]. \tag{A.1}$$

To successfully couple the fundamental mode to the cavity, the beam waist must be positioned in such a way that the radius of curvature of the beam matches these of the mirrors [42]. The plane mirror has $R_1 = \infty$. With Eq. (A.1) it follows that $z(R_1) = 0$ and therefore $w(R_1) = w_0$. This means that the waist needs to be located at the position of the plane mirror. In Fig. A.1 a simplified description of the Fabry-Pérot resonator is shown.

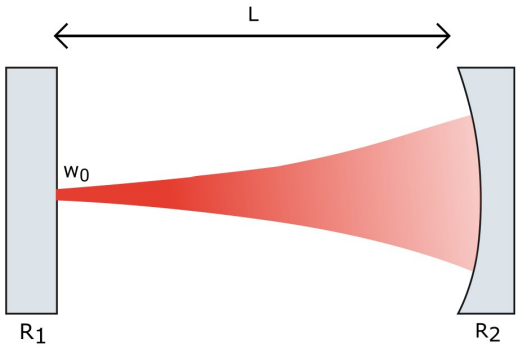

Figure A.1: Simplified description of the Ultra Low Expansion (ULE) resonator used in the HQO experiment for frequency stabilization of the Master Laser. Radius of curvature: $R_1 = \infty$, $R_2 = -500\,\text{mm}$; distance $L = 100.1\,\text{mm}$.

A.2 Adjustment of MOT beam polarization

The six MOT beams have to be circularly polarized. The polarization of the horizontal and vertical beams needs to be of different handedness. A quarter-wave plate can transform the linearly polarized light from the output of the fiber beam splitter into circularly polarized light when the angle between polarization axis of the incident light and optical axis of the QWP is 45°. To adjust the polarization of the MOT beam one additional QWP and a polarizer are needed as a reference. At first only the reference QWP and the polarizer are placed behind the fiber output as shown in Fig. A.2. The reference QWP is rotated until 50% of the incident intensity is detected behind the polarizer what indicates circularly polarized light behind the QWP. Thus, the optical axes of the reference QWP have a 45° to the polarization axis of the incident light. In order to find the right orientation of the first QWP, it is placed in front of the reference optic as shown in Fig. A.2. Two QWPs behind each other can act as a zero–λ–plate, what means that the polarization does not change, or a $\lambda/2$–plate, what causes the polarization axis of the incident light to rotate around 90°. This depends on the orientation of the two QWPs to each other as shown in Fig. A.2. The first QWP is orientated correctly when the intensity behind the polarizer reaches a minimum or a maximum. In this case the QWP creates circularly polarized light instead of elliptical polarized light. The minimum and maximum correspond to circularly polarized light behind the first QWP with opposite handedness. The QWP for the horizontal beams is rotated in such a way that the transmission through the reference optic is maximal. For the vertical beams the QWP is adjusted so that the transmission through the reference optic is minimal. This makes sure that horizontal and vertical MOT beams have different handedness.

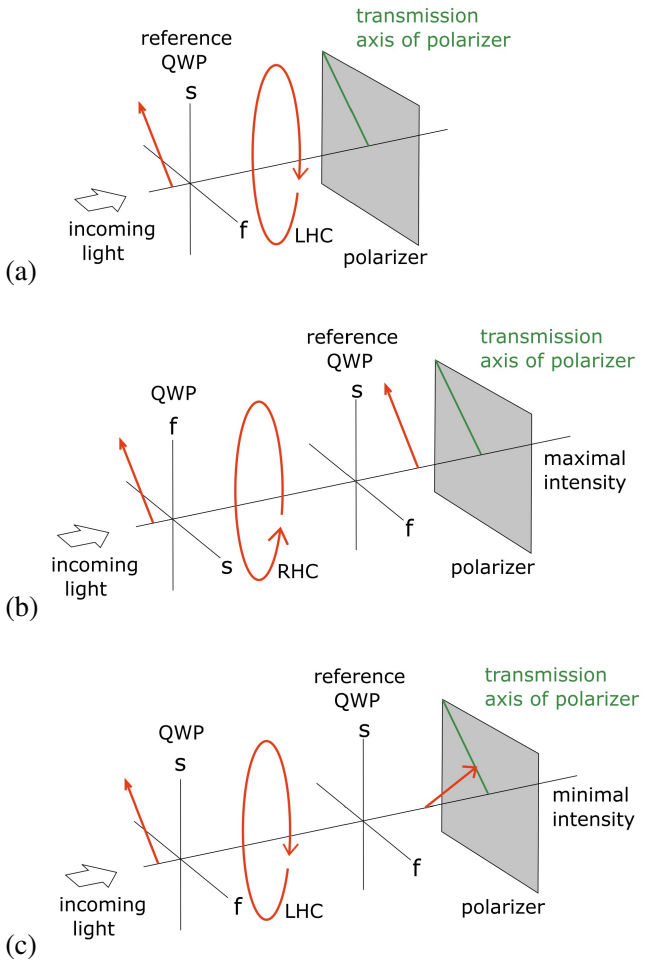

Figure A.2: Schematic representation on how to adjust the polarization of the MOT beams. The fast and slow axes of the quarter-wave plates (QWP) are marked with 'f' and 's'. The red lines indicate the polarization of the light. RHC and LHC describe right– and left–handed circularly polarized light. The green line on the polarizer marks the transmission axis of the polarizer. **(a)** Setup for adjusting the reference optic. The reference QWP is orientated correctly when 50% of the incident light is transmitted through the polarizer. **(b)** Orientation of QWP for creating right–handed circularly polarized light, what corresponds to maximal transmission through the reference optic. **(c)** Orientation of QWP for creating left–handed circularly polarized light, what corresponds to minimal transmission through the reference optic.

A.3 Time of flight (TOF) measurement

The temperature of the atom cloud in the MOT can be measured with the time of flight (TOF) method. When the atoms are released from the trap, they thermally expand and fall down because of gravity. The expansion time of the cloud is defined by the velocity of the atoms, hotter atoms expand faster. Therefore, by determining the velocity of the expanding atoms the temperature can be extracted. This can be done with absorption imaging. The imaging camera may be placed in the (x, y)–plane and the imaging beam is propagating in the z-direction (see Fig. A.3). The velocities of the released atoms are

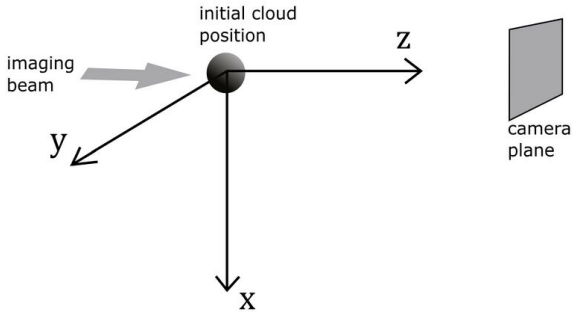

Figure A.3: Coordinate system for the absorption imaging. The camera is placed in the x–y plane and the imaging beam is propagating in z–direction. Image adapted from [62].

Maxwell-Boltzmann distributed. The probability distribution of finding an atom at the initial position x_0 with velocity v_x and initial width σ_0 is given by [62]

$$N(x_0, v_x) = \frac{1}{\sqrt{2\pi\sigma_0^2}} \exp\left\{-\frac{x_0^2}{2\sigma_0^2}\right\} \frac{1}{\sqrt{2\pi\sigma_v^2}} \exp\left\{-\frac{v_x^2}{2\sigma_v^2}\right\}$$

where $\sigma_v = \sqrt{\frac{k_B T}{m}}$, m is the mass of the atoms, k_B is the Boltzmann constant and T the temperature. To get the spatial distribution of the atoms after a time t the velocities can be rewritten in terms of position and time. Integrating over the initial position within infinite limits then leads to a spatial atomic distribution after a time t of the form [62]

$$N(x) = \left(\frac{1}{2\pi\sigma_T(t)^2}\right)^{1/2} e^{-\frac{x^2}{2\sigma_T(t)^2}} \tag{A.2}$$

with

$$\sigma_T(t) = \sqrt{\sigma_v^2 t^2 + \sigma_0^2} = \sqrt{\frac{k_B T}{m} t^2 + \sigma_0^2}.$$

This can be derived similarly for the y–direction.

For actually measuring the temperature T with absorption imaging, several absorption images at a different expansion time t after turning of the MOT have to be taken. By fitting a Gaussian distribution to the absorption images the width σ_T of the distribution that depends on the temperature T and the time t can be obtained. The temperature can then be extracted by plotting $\sigma_T(t)^2$ against the expansion time squared t^2 and fitting a linear function to it.

Bibliography

[1] M. Saffman, T. G. Walker and K. Mølmer, *Quantum information with Rydberg atoms*, Reviews of modern physics **82** (2010) 2313.

[2] O. Firstenberg, C. S. Adams and S. Hofferberth, *Nonlinear quantum optics mediated by Rydberg interactions*, Journal of Physics B: Atomic, Molecular and Optical Physics **49** (2016) 152003.

[3] E. Urban et al., *Observation of Rydberg blockade between two atoms*, Nature Physics **5** (2009) 110.

[4] A. Gaëtan et al., *Observation of collective excitation of two individual atoms in the Rydberg blockade regime*, Nature Physics **5** (2009) 115.

[5] J. A. Sedlacek et al., *Microwave electrometry with Rydberg atoms in a vapour cell using bright atomic resonances*, Nature Physics **8** (2012) 819.

[6] E. L. Raab, M. Prentiss, A. Cable, S. Chu and D. E. Pritchard, *Trapping of neutral sodium atoms with radiation pressure*, Physical review letters **59** (1987) 2631.

[7] *Nonlinear Quantum Optics Group – Hybrid Quantum Optics*, `https://www.nqo.uni-bonn.de/research/hybrid-quantum-optics`.

[8] E. L. Raab, M. Prentiss, A. Cable, S. Chu and D. E. Pritchard, *Trapping of neutral sodium atoms with radiation pressure*, Physical review letters **59** (1987) 2631.

[9] M. Greiner, I. Bloch, T. W. Hänsch and T. Esslinger, *Magnetic transport of trapped cold atoms over a large distance*, Physical Review A **63** (2001) 031401.

[10] T. Nirrengarten et al., *Realization of a superconducting atom chip*, Physical review letters **97** (2006) 200405.

[11] J. Fortágh and C. Zimmermann, *Magnetic microtraps for ultracold atoms*, Reviews of Modern Physics **79** (2007) 235.

[12] J. Fortágh, A. Grossmann, C. Zimmermann and T. Hänsch, *Miniaturized wire trap for neutral atoms*, Physical review letters **81** (1998) 5310.

[13] R. Stevenson, J. Minář, S. Hofferberth and I. Lesanovsky, *Prospects of charged-oscillator quantum-state generation with Rydberg atoms*, Physical Review A **94** (2016) 043813.

[14] K.-N. Schymik et al., *Single atoms with 6000-second trapping lifetimes in optical-tweezer arrays at cryogenic temperatures*, Physical Review Applied **16** (2021) 034013.

[15] I. Beterov, I. Ryabtsev, D. Tretyakov and V. Entin, *Quasiclassical calculations of blackbody-radiation-induced depopulation rates and effective lifetimes of Rydberg n S, n P, and n D alkali-metal atoms with $n \leq 80$*, Physical review A **79** (2009) 052504.

[16] H. Busche, *Efficient loading of a magneto-optical trap for experiments with dense ultracold Rydberg gases*, University Heidelberg, 2011.

[17] E. D. Black, *An introduction to Pound–Drever–Hall laser frequency stabilization*, American journal of physics **69** (2001) 79.

[18] C. J. Foot, *Atomic Physics*, Oxford University Press, ISBN: 978-0-19-850695-9.

[19] P. v. d. S. H. J. Metcalf, *Laser Cooling and Trapping*, Springer-Verlag, ISBN: 0-387-98728-2.

[20] Y. H. Fung, P. Sompet and M. F. Andersen, *Single atoms preparation using light-assisted collisions*, Technologies **4** (2016) 4.

[21] D. A. Steck, *Rubidium 85 D line data*, https://steck.us/alkalidata/rubidium85numbers.pdf, visited on 14.01.2023, 2021.

[22] D. A. Steck, *Rubidium 87 D line data*, https://steck.us/alkalidata/rubidium87numbers.pdf, visited on 14.01.2023, 2021.

[23] S. L. Cornish, N. R. Claussen, J. L. Roberts, E. A. Cornell and C. E. Wieman, *Stable 85 Rb Bose-Einstein condensates with widely tunable interactions*, Physical Review Letters **85** (2000) 1795.

[24] A. Banerjee, D. Das and V. Natarajan, *Precise fine-structure and hyperfine-structure measurements in Rb*, arXiv preprint physics/0209019 (2002).

[25] J. Gamper, *Frequenzstabilisierung zur Laserkühlung von Rubidium*, Rheinische Friedrich-Wilhelms-Universität Bonn, 2022.

[26] *VACOM*, https://www.vacom.net/de/home.html, visited on 14.01.2023.

[27] *PFEIFFER VACUUM Turbopumpen*, https://www.pfeiffer-vacuum.com/de/produkte/vakuumerzeugung/turbopumpen/, visited on 14.01.2023.

[28] *SAES GETTERS NEXTorr Z 200*, https://www.saesgetters.com/sites/default/files/NEXTorr%20Z%20datasheets.pdf, visited on 14.01.2023.

[29] *AlfaVakuo e.U. Metal Vapour Sources*, https://alfavakuo.eu/products/mvs/, visited on 14.01.2023.

[30] *DELTA ELEKTRONIKA*, https://delta-elektronika.nl/, visited on 21.01.2023.

[31] W. Demtröder, *Experimentalphysik 2 - Elektrizität und Optik*, vol. 2, Springer, 2004.

[32] B. Jagatap, K. Manohar, S. Nakhate, A. Marathe and S. Ahmad, *Magneto-optical traps for neutral atoms*, Current Science (1999) 207.

[33] L. Ricci et al., *A compact grating-stabilized diode laser system for atomic physics*, Optics communications **117** (1995) 541.

[34] *Tunable Diode Lasers UV, Visible, Infrared - Digital Control - Wavelength Stabilization*, https://www.toptica.com/fileadmin/Editors_English/11_brochures_datasheets/01_brochures/toptica_BR_Scientific_Lasers.pdf, visited on 10.01.2023.

[35] À. Wenxian, *Design and characterization of a littrow configuration external cavity diode laser*, The Board of Trustees of the Center for Excellence in Education () 21.

[36] *TOPTICA TA pro Tapered Amplifier Laser System*, https://www.toptica.com/products/tunable-diode-lasers/amplified-lasers/ta-pro, visited on 10.01.2023.

[37] *HighFinesse WS6-200 Series High Precision Wavemeter*, https://www.highfinesse.com/en/wavelengthmeter/wavelengthmeter-ws-6-200.html, visited on 04.01.2023.

[38] W. Demtroeder, *Experimentalphysik 3 - Atome, Moleküle und Festkörper*, Springer-Verlag, ISBN: 978-3-662-49093-8.

[39] D. W. Preston, *Doppler-free saturated absorption: Laser spectroscopy*, American Journal of Physics **64** (1996) 1432.

[40] J. Alda, *Laser and Gaussian beam propagation and transformation*, Encyclopedia of optical engineering **999** (2003).

[41] *Stable Laser Systems Vacuum Housing 6010/6020*, https://stablelasers.com/wp-content/uploads/2017/06/6010_20_R1.pdf, visited on 17.01.2023.

[42] R. W. Fox, C. W. Oates and L. W. Hollberg, "1. Stabilizing diode lasers to high-finesse cavities", *Experimental methods in the physical sciences*, vol. 40, Elsevier, 2003 1.

[43] *EOSpace*, https://static1.squarespace.com/static/5b4391a0a2772c7a5b0dae43/t/61eeea325bcf5e5c96f55a06/1643047476220/EOSPACEbriefProductInfo2022.pdf, visited on 17.01.2023.

[44] *Windfreak Technologies, LLC*, https://windfreaktech.com/, visited on 09.01.2023.

[45] *TOPTICA Fast Analog Linewidth Control FALC pro*, https://www.toptica.com/products/tunable-diode-lasers/laser-locking-electronics/falc-pro, visited on 09.01.2023.

[46] B. Heinrich and W. Schneider, *Grundlagen Regelungstechnik*, vol. 5, Springer, 2019.

[47] K. Balakier, L. Ponnampalam, M. J. Fice, C. C. Renaud and A. J. Seeds, *Integrated semiconductor laser optical phase lock loops*, IEEE Journal of Selected Topics in Quantum Electronics **24** (2017) 1.

[48] *ANALOG DEVICES High Frequency Divider/PLL Synthesizer ADF4007*, https://www.analog.com/media/en/technical-documentation/data-sheets/ADF4007.pdf, visited on 21.01.2023.

[49] J. Appel, A. MacRae and A. I. Lvovsky, *A versatile digital GHz phase lock for external cavity diode lasers*, Measurement Science and Technology **20** (2009) 055302.

[50] *Ultrafast MSM photodetector G4176-03 Hamamatsu*, https://www.datasheets360.com/pdf/-5073308062623184073, visited on 04.01.2023.

[51] P. Florian, *Aufbau, Optimierung und Charakterisierung von frequenzstabilisierten Lasersystemen*, Rheinische Friedrich-Wilhelms-Universität Bonn, 2022.

[52] M. Duocastella, S. Surdo, A. Zunino, A. Diaspro and P. Saggau, *Acousto-optic systems for advanced microscopy*, Journal of Physics: Photonics **3** (2020) 012004.

[53] D. Meschede, *Optik, Licht und Laser*, Vieweg+Teubner, ISBN: 978-3-8351-0143-2.

[54] *Gooch & Housego AOMO 3080-122*, https://gandh.com/products/acousto-optics/modulators/aomo-3080-122, visited on 06.01.2023.

[55] *Evanescent Optics Inc. Spliceless PM Coupler arrays*, http://www.evanescentoptics.com/products/?id=20, visited on 09.01.2023.

[56] W. Ketterle, D. S. Durfee and D. Stamper-Kurn, *Making, probing and understanding Bose-Einstein condensates*, arXiv preprint cond-mat/9904034 (1999).

[57] T. Pyragius, *Developing and building an absorption imaging system for Ultracold Atoms*, arXiv preprint arXiv:1209.3408 (2012).

[58] *pco.pixelfly usb CCD camera*, https://www.pco.de/fileadmin/user_upload/pco-product_sheets/pco.pixelfly_usb_data_sheet.pdf, visited on 07.01.2023.

[59] *Thorlabs AC508-100-B*, https://www.thorlabs.com/thorproduct.cfm?partnumber=AC508-100-B.

[60] *Thorlabs AC508-200-B*, https://www.thorlabs.com/thorproduct.cfm?partnumber=AC508-200-B.

[61] H. Tore, *Computer Control System for Cold Atom Experiments*, Rheinische Friedrich-Wilhelms-Universität Bonn, 2022.

[62] T. M. Brzozowski, M. Maczynska, M. Zawada, J. Zachorowski and W. Gawlik, *Time-of-flight measurement of the temperature of cold atoms for short trap-probe beam distances*, Journal of Optics B: Quantum and Semiclassical Optics **4** (2002) 62.